University of Utrecht

Debye Institute

Atoms Optics and Ultrafast Dynamics

A stereo-tweezer for ultracold atoms

Author:
Zimma Kluit

Supervisors:
Dr. D. van Oosten
Msc. S. Pratama

November 2013

Abstract

The Atom Plasmonics group plans to study the interactions between Rubidium atoms in the near-field of nanostructures. For these experiments an optical tweezer is needed to move the trapped atoms above a gold surface. To transfer the atoms to the surface, this tweezer must actually be a standing wave. Thus, a second tweezer should be overlapping with the first. This stereo tweezer or scanner will consist of two pairs of scanning mirrors that move the trapping beam in the plane above the surface. In this thesis the design and the performances of this stereo scanner in one dimension was tested.

To implement the scanner, standard galvo scanning mirrors were used as is typically done in confocal scanning microscopy. However, two problems arise with the use of these galvos. First, the electronic feedback that controls the angle of the mirror, introduces noise in the angle and thus in the position of the trap. As a result, a bump arises in the spectrum of the noise. By tuning the constants of the controller of the galvos, this bump was decreased.

Second, the two beams should remain overlapped even when the mirrors are scanning. This was achieved by measuring the difference in angle between the galvos and correcting the angle of one of them using a feedback loop. This method was tested by coupling light that has pasted over both galvos back into a single-mode fiber. If the feedback system works the light should remain coupled in the fiber even when the mirrors are scanning. Remaining fluctuations in the fiber coupling were found to be dominated by movements of the beam orthogonal to the scanning axis.

Contents

1

Introduction

The field of plasmonics has a long history, even if the name was invented relatively recently[1]. In 1902 Wood observed unexplained features in optical reflection measurements on metallic gratings[2]. More than fifty years later Pines theoretically described the characteristic energy losses experienced by fast electrons traveling through metals[3]. Those losses were ascribed to collective oscillations of free electrons in the metal and got the name 'plasmons'. Coupled oscillations of bound electrons and light inside a transparent medium are called a 'polariton'[4].

In 1957 Ritchie investigated the electron energy losses in thin films and showed plasmon modes were able to exist close to a metal surface. This theoretical description is the first on 'surface plasmons'[5, 6]. The theory was later verified with electron energy-loss experiments and more research[7, 8, 9].

The *nanoplasmonics* field is gaining attention for the development of the excitation and manipulation of surface plasmons created by subwavelength sized structures in metal films. The ambition of this field is to manage properties of light to make new optical element for sensing applications and for example communication.

In the field of *ultra cold atoms*, magnetic fields and laser light are used to control and manipulate atoms in traps. Big successes were achieved with the ability to control with very high accuracy the internal and external state of atoms in the gas phase [10]. This control makes ultracold atoms a beautiful field to study problems in condensed matter, quantum information processing and cavity quantum electrodynamics.

In our experiment these two interesting fields will be combined. By trapping atoms in the near-field of a plasmonic nanostructure, we will be able to control and study the coupling between atoms and light close to the structure.

A hot topic in nanoplasmoncis is the study of manipulation of light by sub-wavelength sized holes in metal films. When light is focussed on a small hole, the light is diffracted into a spherical wave. It was shown that a periodic grating in the surface of the film modify the transmission pattern of this hole[11]. The divergence of this pattern was shown to be less than 5°. This beaming of light is ascribed to surface plasmons, excited at the hole, efficiently radiate as light due to the concentric rings.

A nanohole array was found to exhibit an extraordinarily high optical transmission with suitable chosen wavelength of the light and spacing of the array[12]. The presence of atoms in the array gives an extra periodic modulation of the index of refraction. This will be used to control the interaction between light and plasmonic modes and will thereby influence the transmission of the array[13]. Since the transmission of the light is tightly diverging, in the experiment it could be used to create micro traps[14] for atoms.

With that in mind, our experiment requires three things: ultra cold atoms, a nanoplasmonic sample and a means to reproducibly position the atoms on the samples. A vapour of Rb-87 atoms is created in a oven. A 2D-magneto-optical trap (MOT) collects the atoms from this vapor and cools and confines them in two dimensions [15, 16, 17, 18]. This cigar shaped cloud of atom is pushed into a 3D-MOT chamber. In a 3D-MOT atoms are confined in the middle of a vacuum chamber in three dimensions.

The nanostructure can not be placed in the middle of the vacuum chamber, as this would block the lasers required for laser cooling, so the atoms must be moved towards the sample. Therefore, the cold atoms are loaded from the MOT to an optical dipole trap[19]. When the atoms are trapped in the dipole trap, the focus will be moved towards the sample with the atoms in it. When the atoms are positioned above the sample, they must be lowered. Therefore a 1D-optical lattice[21] is required to move them in the vertical direction. This optical *conveyor*[22] will be created by a standing wave[23] consisting of two counter propagating laser beams.

This brings us to the unique and most challenging part so far. Since we want to move the atoms in two dimensions above the sample, the conveyor should not only move vertically towards the plane of the sample, but also in the plane of the sample. This means the standing wave needs to be produced by two counter propagating laser beams that can move sideways but remain perfectly overlapped and parallel to each other at all times.

In this thesis the design and the realization of this so-called scanner will be discussed and tested. In Chapter 2 the setup of the experiment will be described. The design and devices for the cold atoms will be shown first. Then the setup of the scanner will follow.

Chapter 3 provides a theoretical background. The optical lattice and the errors from an achromatic lens will be discussed. The theory behind control

systems will be presented as well.

Three tests on the scanner are introduced in Chapter 4. High frequency oscillations, the so-called servobump are decreased in the first test experiment. Secondly the overlap error is minimized by introducing a PI-controller to the system.

In Chapter 5 the conclusions of the test experiments are given.

This chapter introduces the setup of the experiment. First the cooling and trapping devices will be described, then we will continue with the scanner. In figure 2.1 a schematic representation is given of the setup.
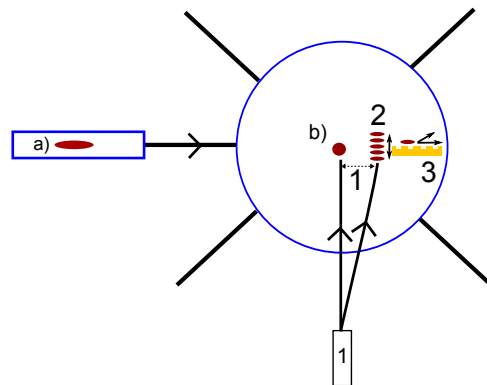

Figure 2.1: The setup of the experiment with the cloud of atoms in a) the 2D-MOT and b) the 3D-MOT. 1,2 and 3 refer to respectively the optical tweezer, conveyor and the scanner. Outside the chamber four of the six beams of the 3D-MOT are shown, a push beam and two possible tweezer beams.

As discussed in the introduction we start with a 2D-MOT (with a pressure of 10^{-7} mbar) to cool and trap atoms in a cigar shaped cloud. The cigar shaped cloud is easy to push into the vacuum chamber where the atoms will be confined in three dimensions in a 3D-MOT. The maximum number of atoms in the 3D-MOT is around 10^{10} [25]. The nanostructure is not placed in the center of the vacuum chamber, because it would intersect

with the MOT-beams. After loading the atoms from the MOT, they are loaded into the optical tweezer[19]. This tweezer is a strongly focussed 20 Watt laser beam with a wavelength of 1070 nm. The beamwaist is 47 μm in the vertical direction to 81 μm [27] in the horizontal direction, where the directions are defined as in figure 2.1. The used forces come from the electric dipole interaction with far-detuned light. The trap depth in our setup is around 2mK. By moving the focus of the tweezer, the cloud is be moved towards the sample. A special rotating arm moves the laser such that the atoms will move in a straight line close to the sample. The mechanism of this arm is not trivial, because it should move in a straight line instead of an arc. The optical tweezer is working and the details are discussed elsewhere [26].

To get the atoms to a height of a few 100 nm above the sample, an optical conveyor is installed. The apparatus consists of two counter propagating overlapping laser beams; the first is incident from above and the second from the bottom. Those two beams will result in a periodic standing wave potential, in which the cloud will be trapped in a pancake shaped clouds. When we choose a red detuning, atoms will be trapped at the antinodes of the standing wave, which are half a wavelength apart. In section 3.1 this so-called optical lattice will be explained.

By shifting the frequency of one of the beams of the standing wave, the anti-nodes of this standing wave will move and therefore move the cloud of atoms in vertical direction. In figure 2.2 a simplified model is shown of the conveyor. The optical lattice consists of a waist of approximately 75 μm and a lattice spacing of around 400 nm. The conveyor is investigated[27] and will soon be installed and tested.
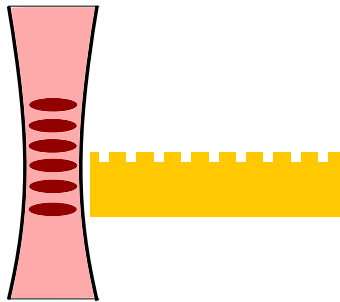

Figure 2.2: The optical conveyor close to the sample. An optical lattice of a few pancakes formed by two overlapping beam.

7

Once the atoms are trapped above the sample, the laser beam from below can be switched off, as the reflection of the upper laser beam on the sample will create a standing wave in the overlapping area. This standing wave will form a trap for the atoms. By varying the angle of the incoming beam, one can even change the distance between the atoms and the surface. This allows investigation of the coupling between atoms and nanostructures. Imaging will take place with a beam from above using absorbtion at 780 nm or possibly fluorescence at 420 nm to achieve a higher spatial resolution. The beam from below can be used for different purposes when taking measurements. For example the beam can be used to create micro traps where the atoms could be trapped. Surface plasmons could also be manipulated by shooting light on another structure than the imaged structure. The image could give us information on the effect of the holes on surface plasmons. When the atoms are trapped that close to the surface of a nanostructure, there are a lot of interesting experiments possible to measure the influence of the atoms on the surface plasmons and visa versa.

2.1 Scanner

The scanner is used for two things: to transfer the atoms from the original conveyor to the standing wave produced by the sample and to subsequently move the atom around above the sample. For the second part only the beam from above will be used. The scanner uses the same optics as the conveyor; the same laser beams that will translate the atoms vertically, will move them in the horizontal plane above the surface in two dimensions. The setup of the scanner and conveyor consists of two horizontal and one vertical part that are mounted in the coloured frame given in figure 2.3a. The horizontal parts are the arms at the upper and lower level, while the vertical part is positioned between both levels. The horizontal parts contain two achromatic lenses and two galvos. Galvos are rotating mirrors that will be discussed in section 4.1 in more detail. The top level has the same components as the lower level figure of figure 2.4, but is extended with some imaging and devices for measuring.

The vertical part contains of the sample and two lenses and is represented in figure 2.3b. The beams from the upper and lower level will meet the sample in this vertical part.

upper level

vertical part

lower level

Galvo 2
at upper level

Galvo 2
at lower level
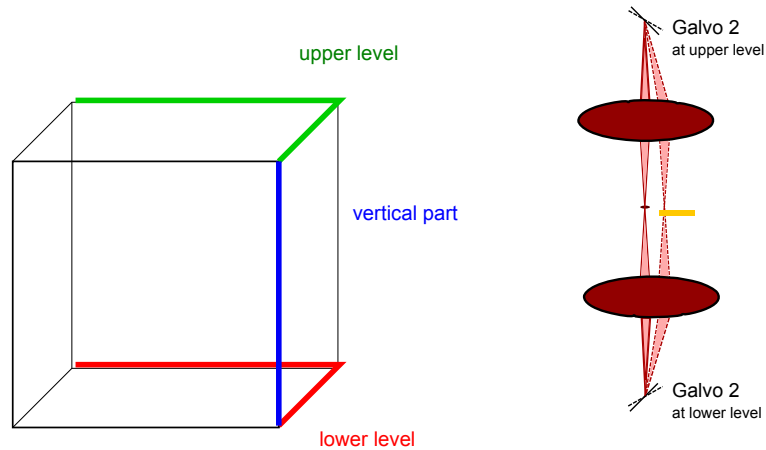
(a) This frame of the scanner is a tool to visualize the construction of the scanner. In the red part the lower arm will be place, even as the upper arm in the green part and the vertical part on the blue axis.

(b) The vertical part of scanner with the atom cloud and the sample at the focus of the lens. The dashed lines show the beam path when the galvos makes a non-zero angle. The rotation of this pair of galvos introduces a movement in only one dimension.

The four galvos are split into to pairs, the first pair of galvos will move the focus in the x-direction, while the other pair will move in the y-direction. We define the galvos 1 to move the beam in the x-direction and the galvos 2 in the y-direction.

On the horizontal levels one of both galvos will be installed, to get the desired movements at the sample.
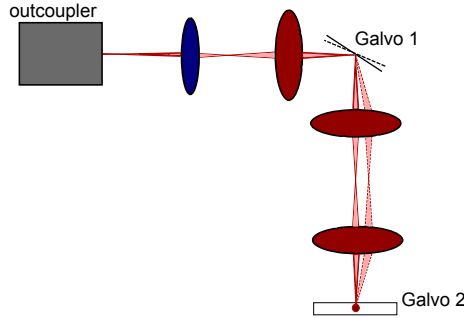
Figure 2.4: The horizontal levels of the setup contain an outcoupler, two galvos and four achromatic lenses. Galvo 2 is pointed into or away from the plane of the paper. Rotations of galvo 1 and galvo 2 are responsible for movements in two dimensions. On the top level also measuring and imaging devices will be installed.

To clarify the procedure of moving the cloud, only one pair of galvo is considered. Between the two galvos two achromatic lenses are positioned. The distance between one galvo and one achromat is the focal distance of the lens. After a beam hitting the first galvo and the first lens, it will propagate parallel to the optical axis. After twice the focal distance, the beam will hit the second galvo and travel on the optical axis. This is independent of the angle of the galvo. However when moving the first galvo to a certain angle, the beam will move a certain distance perpendicular to the optical axis after the first achromatic lens. At the focus of the beam, at focal distance from the lens, the atoms will be trapped and moved in one direction. The beams trapping the atoms should at this point overlap accurately. In the test experiments of chapter 4 only consider half of the scanner is considered, which can be extended with two galvo pairs and therefore to two dimensions.

2.1.1 Scanner Design

The technical design of the scanner in the experiment looks more complicated than the sketch. In the end three levels in the experimental setup are required, shown in figure 2.6 and 2.7.
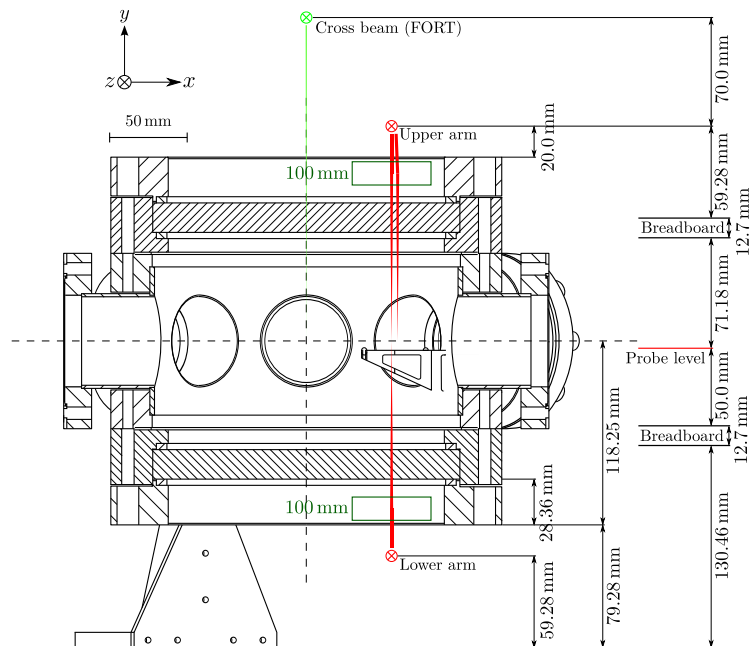Figure 2.5 shows the heights of those different levels.

Figure 2.5: The experimental setup of the vacuumchamber with the different heights for the scanner and conveyor [27].

In figure 2.5 the vacuum chamber is represented with the different levels. Just below the middle of the height of the chamber an arm is shown for the sample. From above three beams and from above one beam is shown coming from the two levels. One each level consists of one galvo 1 and one galvo 2, together with the appropriated achromatic lenses.
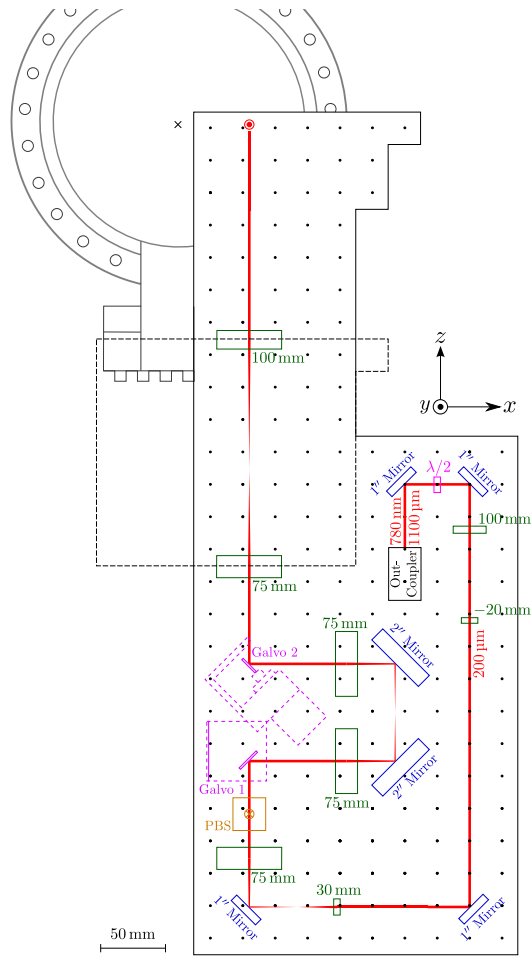
Figure 2.6: The experimental setup of the bottom level[27].

The top layer consists of the other two galvos and achromats, the controlling and imaging system. The galvos are placed exactly in the same way as on the bottom layer.
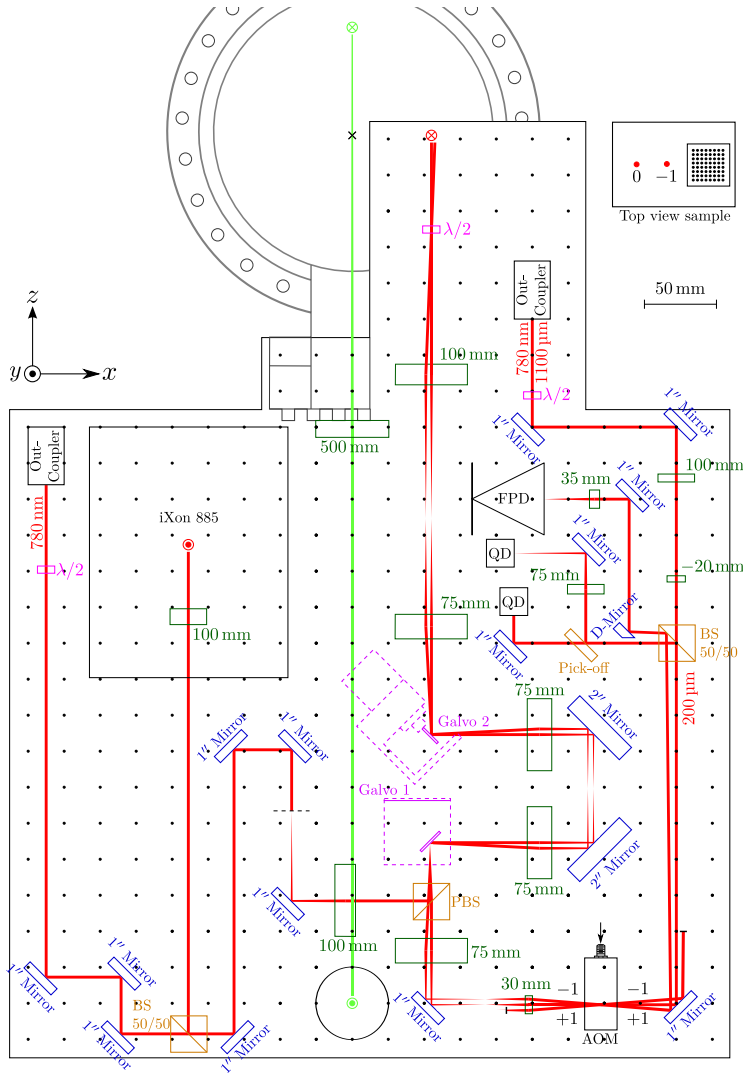
Figure 2.7: The top level of scanner and conveyor, with control and measure devices[27].

Vertical movement   Because of spatial constraints, galvo 2 is positioned differently than the first one. The rotation axis of the galvo lies in the plane of the beam. The rotation of the galvo results in a vertical movement of the beam in the image plane which is perpendicular to the propagation direction of the beam. This vertical movement however has also a component in the x-direction. In figure 2.8 the situation is shown in our coordinate system. The z-coordinate is defined along the beam, the x-coordinate is in the horizontal plane, while the y-coordinate represents the vertical plane. The movements in the image plane are given in x- and y-coordinates.
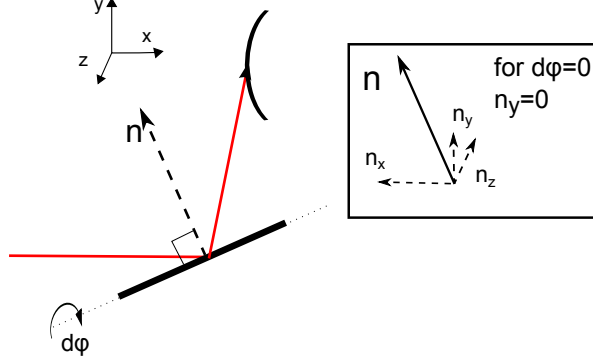
Figure 2.8: A rotation of the second galvo will not only introduce a vertical movement, but also a movement in the horizontal direction. By decomposing the vectors of the normal, one finds out that the x- and z-movements are also dependent on the rotation angle $d\phi$.

Since the rotation axis lies in the x-z plane, a $d\phi$ rotation moves the normal out of this plane. The normal vector component in the x-z plane will become smaller. This automatically means the component increases in other planes. Therefore we will decompose the normal vector in three components in the given three dimensions of figure 2.8.

$$n_x = n_0 \cos\theta \cos d\phi, \qquad (2.1a)$$

$$n_y = n_0 \sin d\phi, \qquad (2.1b)$$

$$n_z = n_0 \sin\theta \cos d\phi, \qquad (2.1c)$$

where n_0 is the original length of the normal vector and θ is the angle between the normalvector and the incoming beam in the x-z plane. When $d\phi$ is zero, there will only be a y-component in the x-y (image)plane. The θ is fixed in this plane, so will introduce a factor $\sqrt{2}$ in both x and z-components. If the components of the normal vector are dependent on the rotation angle, the outcoming angle of the beam is as well. Since we are reflecting the beam, the x-coordinate will be transformed into a negative x-coordinate.

When constructing the path of the beam when rotating $d\phi[-\frac{\pi}{2}, \frac{\pi}{2}]$, we will find an elliptic shaped path. The x-direction is tightened with a factor $\sqrt{2}$ with respect to the y-movement. This complicates positioning atoms on the sample, but also couples the feedback loops for the vertical and horizontal position. We have not tested the feedback loop in this configuration yet.

Theoretical Background

In this chapter we first give a theoretical background on optical lattice. We will then present the calculations of the imperfections caused in a real setup by the use of non-perfect lenses. Finally we will give an introduction to control systems, as this will also be used throughout the thesis.

3.1   1D optical lattice

To understand the conveyor we will provide the basic theory of the optical lattices [21].
In the experiment we work with laser light from a diode laser, which is delivered to the experiment through a single mode optical fiber. This means that both the electric field and the intensity of the light beam can be extremely well approximated by a gaussian distribution.

We define r as the distance from the optical axis, z as the axial distance from the focus of the beam and k as the wave number.
We can then write the electric field of a gaussian beam as

$$E(r,z) = E_0 \frac{w_0}{w_z} \mathrm{e}^{\left[\frac{-r^2}{w^2(z)} - ikz - \frac{ikr^2}{2R(z)} + i\zeta(z) \right]}, \tag{3.1}$$

where w_0 is the waist in the focus, $w(z)$ waist elsewhere along the beam and R(z) is the radius of curvature at a position along the beam. $\zeta(z)$ is the longitudinal phase delay or Gouy phase. The Gouy phase shift acquires an extra π-phase shift for a gaussian beam that is going through the focus.

The intensity of light can be written as $I(r,z) = \frac{1}{2} c \epsilon_0 |\mathrm{E}|^2$. The power P of the beam is given by $P_0 = \frac{1}{2} I_0 \pi w_0^2$, where I_0 is the peak intensity in the focus.

The intensity in the beam is then given by

$$I(r,z) = I_0 \left(\frac{w_0}{w(z)} \right)^2 e^{\frac{-2r^2}{w(z)^2}}, \tag{3.2}$$

If we rewrite all those equations in terms of the total power P of the beam we find

$$I(r,z) = \frac{2P}{\pi w(z)} e^{\frac{-2r^2}{w(z)^2}}, \tag{3.3}$$

where we used the fact that for a gaussian beam $w(z) = w_0 \sqrt{1 + (\frac{z}{z_R})^2}$. An optical 1D-lattice is a standing wave formed of such gaussian beams with a frequency far from the atomic resonance. The beams should ideally have identical waists and focal points and should of course be counter propagating.

The reason the standing wave acts as a potential is that the electric field of light induces a dipole moment $p = \alpha E$, which in turn experiences a potential $U = -pE$ to the same electric field. As the dipole moment is induced by E, we should actually include a factor of $\frac{1}{2}$.

$$U_{\text{dipole}}(\vec{r}) = -\frac{1}{2}\alpha(w) \mid E \mid^2 = -\frac{\pi c^2}{2\omega_0^3} \frac{\Gamma}{\Delta} I(r), \tag{3.4}$$

where Δ is the effective detuning and Γ the linewidth of the relevant transition. Both these quantities are dependent on the atomic level structure; in the case of ^{87}Rb-atoms, there are two relevant transitions. Those transitions are from the ground state $5S_{1/2}$ to the excited $5P_{1/2}$ level (794.98 nm) or to the excited $5P_{3/2}$ level (780.24 nm).

For two counter propagating beams the intensity of the standing wave is obtained from

$$
\begin{aligned}
I(r,z) &= |\sqrt{I_1}e^{ikz} + \sqrt{I_2}e^{-ikz}|^2 \frac{w_0^2}{w_z^2} e^{-2\frac{r^2}{w^2}} \\
&= (I_1 + I_2 + 2\sqrt{I_1 I_2} \cos 2kz) \frac{w_0^2}{w_z^2} e^{-2\frac{r^2}{w^2}},
\end{aligned} \tag{3.5}
$$

where I_1 and I_2 are the intensities of the two beams. When the intensities of the beams are equal $I_1 = I_2 = I_0$, we find

$$
\begin{aligned}
I(r,z) &= 2I_0(1 + \cos 2kz) \frac{w_0^2}{w_z^2} e^{-2\frac{r^2}{w^2}} \\
&= 4I_0(1 - \sin kz^2) \frac{w_0^2}{w_z^2} e^{-2\frac{r^2}{w^2}} \\
&= 4I_0 \cos kz^2 \frac{w_0^2}{w_z^2} e^{-2\frac{r^2}{w^2}}.
\end{aligned} \tag{3.6}
$$

From Equation (3.4) we obtain the potential of the optical lattice

$$U(r,z) = \frac{\pi c^2}{2w_0^3}\frac{\Gamma}{\Delta}4I_0\cos kz^2(\frac{w_0^2}{w_z^2})e^{-\frac{2r^2}{w^2}},$$

$$= U_0\cos kz^2(\frac{w_0^2}{w_z^2})e^{-\frac{2r^2}{w^2}},$$

(3.7)

where the total trap depth $U_0 = 4I_0\frac{\pi c^2}{2w_0^3}\frac{\Gamma}{\Delta}$. For r$<<$ w_0, we can make a Taylor expansion which leads to $U(r,z) = -U_0(1 - 2r^2/w_0^2)\cos kz^2$. In future experiments a trap depth of around 100 μK will likely to be used. The values in power and detuning still need to be chosen. The power we can use is limited to what the sample can stand. The detuning then has to be chosen low enough such that the required depth can be obtained. A lower detuning however automatically means a lower lifetime, which of course is not desirable. The natural linewidth of Rb-87 is (2π)6.06 MHz, while the power will be in the order of 25 mW and the detuning a few nanometers. When an atom has a small displacement with respect to the center of the local potential minimum we can approximate $U = \frac{1}{2}mr^2\omega_r^2 + \frac{1}{2}mz^2\omega_z^2$,

$$\frac{2r^2U_0}{\omega_0^2} = \frac{1}{2}mr^2\omega_r^2 \Rightarrow \omega_r = \sqrt{\frac{4U_0}{m\omega_0^2}}.$$

(3.8)

and

$$\frac{U_0}{z_r} = \frac{1}{2}mz^2\omega_z^2 \Rightarrow \omega_z = k\sqrt{\frac{2U_0}{m}}.$$

(3.9)

We find trap frequencies ω_r=831 Hz and ω_z=177 kHz for our setup.

3.2 Errors from Thick Lenses

As described in the introduction of the thesis the optical lattice described above will be scanned sideways i.e. perpendicular to the z-axis. This means the beam will not always pass through the center of the lenses. To minimize errors caused by this fact, we use achromatic lenses. In the following, we will discuss the errors that we can expect from the thick lenses.

An achromatic lens corrects for effects called spherical aberration and dispersion. Spherical aberration causes a not so well defined focal length when hitting the lens at different heights. Dispersion is the phenomenon of the phase velocity of a wave depending on its frequency. This means the refractive index changes with the wavelength of the light shooting through the material.

Dispersion can lead to chromatic aberration, which results in blurred

images. Chromatic aberration is the effect of a lens having different focal distances for different wavelengths. The outcoming angle of the beam will therefore be different for the different wavelengths.

Achromatic lenses are designed to correct for this effect and contain two parts of different sorts of glass. The glass sorts and thicknesses are chosen, such that the chromatic aberration effect disappears. We end up with achromats that have the property of focussing light of different wavelength in the same point. This is important because the lattice beams need to be focussed at the same position as our probe beams which have different wavelengths.

To investigate the errors we will consider a small part of the setup of the experiment as illustrated in figure 3.3. The setup contains galvo 1 and galvo 2 at a certain position, making respectively angle ω_1 and ω_2. Secondly it consists of two achromatic -also called thick- lenses. Thirdly there are two important points: point F and point P. Point F is the focus of the beam where the atoms will be moved in the direction perpendicular to the optical axis. Point P is an interesting point since in the end the error will be measured at this point. We will come back to this point soon.
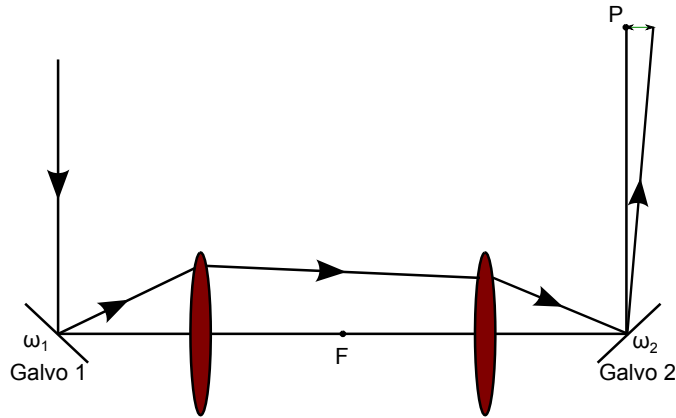

Figure 3.1: The setup and beam path for which the deviations at point F and P will be calculated. The thick lenses introduce an error perpendicular to the optical axis along the path of the beam.

The first two achromats from figure 3.3 are identical. Due to the first achromatic lens the light will not propagate perfectly parallel to the optical axis. The small deviation angle from this fact results in deviations along the ideal path at both point F and P. The deviation at points F and P depends on the angle ω_1 which will be between 0 and 4° in our experiment. The sec-

ond galvo is positioned at an angle ω_2, where in the ideal case holds $\omega_2 = \omega_1$.

This deviation angle after the first achromat has two important consequences; a different lattice spacing and a different overlap region of the counter propagating beam. Since the light propagation distance to point F will be larger with this angle, the lattice spacing of the standing wave will be different as well. This modified lattice spacing is given by $a = \lambda/(2\cos\theta)$, where θ is the deviation angle.
The second same achromat will introduce the same deviation angle for counter propagating beams, so a smaller overlapping region will be introduced. An example of this overlap region at point F is shown in figure 3.2.
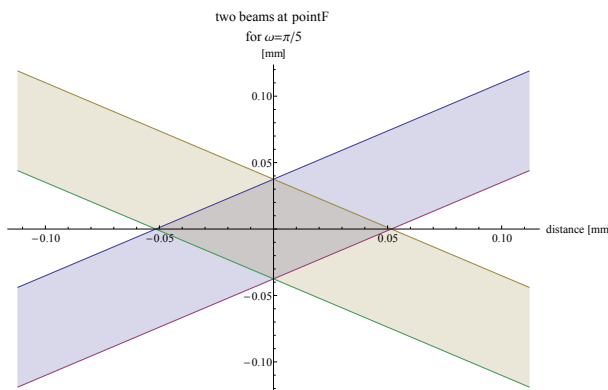

Figure 3.2: The overlap region of two overlapping beams for z_R=5.6 mm and ω_g=π/5.

However, an optical lattice will only be created when the intensity of the beam is high enough and the beams will overlap. The optical lattice will therefore be restricted by the overlap region, which will be discussed in subsection 3.2.2.

Now we will come back to the error at point P. The errors at point P contain the errors from two different causes. The first errors are obtained by the thick lenses in the setup, which are discussed above. The second cause of errors at point P is the difference in angle between the first and second galvo. This unsynchroniety in position will cause an angle with respect to the optical axis at the second galvo and result in an error at point P.
One important difference between those errors is that the unsynchroniety of the mirrors is undesired, while the thick lens error we do not want to cancel. The error of the thick lens we do not want to cancel, because if we do cancel it, the position of the second galvo should be changed and will therefore change the path of a beam counter propagating. Changing the back coming path automatically introduces a change in the overlap region

and thus optical lattice, which we do not want. The unsynchroniety of the galvos we want to cancel to obtain overlapping beams. This will in practice be done in chapter 4.

This brings us back to a small problem at point P, where we will measure both errors. In the end the measurement of the error at point P will be used to cancel the error of the unsynchronized galvos. Now we still capture both errors, so a tool is needed to distinguish both errors. This tool is found to be the third (blue lens) lens in figure 3.3. The third lens captures only the error from the unsynchronized galvos.
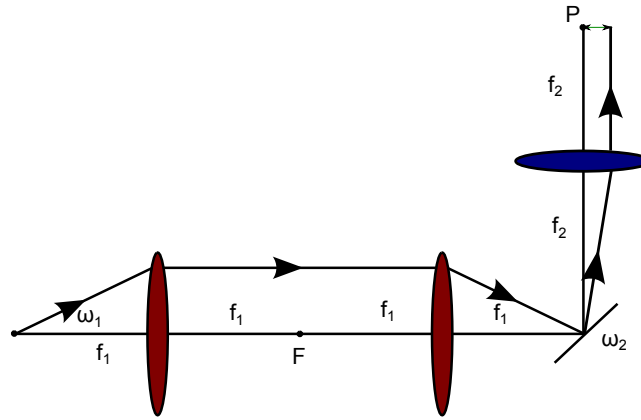

Figure 3.3: The beam path for which the deviations at point P will be calculated. The galvos are unsynchronized since $\omega_1 \neq \omega_2$. The beam at F does not propagate parallel to the optical axis due to the thick lenses. Both deviations will result in the error at point P.

By eliminating this error the situation will be approached by the setup with only thin lenses. The use of thin lenses results in the outcoming beam from the mirror propagating parallel to the optical axis. To summarize, this third lens captures only the desired error and will therefore be really useful. In section 3.3.2 the proof will be given of the third lens indeed doing what it is supposed to do.

3.2.1 Method

The calculations were made with the following procedure. Each intersection of the ray hitting a surface of figure 3.3 and 3.4, gives us a point in our coordinate system. The x-coordinate gives the travel distance of the ray and the y-coordinate is the distance to the optical axis. Due to the different materials through which the ray propagates, the ray will refract. Those points are the intersections for which the coordinates (x,y) were calculated

by solving two equations. The first equation contains the y-coordinate, which is a function of the height and the outcoming angle of the previous coordinate. The second equation for the y-coordinate is a function of the curvature of the (lens) surface. By solving those two equations for x and y, the behaviour of the ray can be reconstructed.
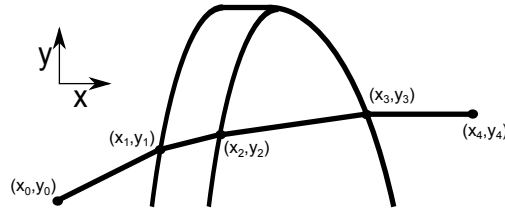

Figure 3.4: The achromatic lens with the intersections of the linear functions with the curvature functions of the surfaces of the lens.

To give an example, the first intersection is given by the linear function $y_1 = x_1 \tan \omega$. The formula for the curvature of the surface of the lens looks as follows: $y_1 = \sqrt{R^2 - (R - x_0 - x_1)^2}$. R is the radius of curvature of the lens. Those two functions intersect at point 1 with intersection coordinate (x_1, y_1). All equations for the coordinates are given in Appendix C "Thick Lens".

The same procedure is used to find the front focal distance of the achromats. The values and equations are in the Appendix A "find front focus".

3.2.2 Results

At first the errors at different points in the setup will be discussed. We will continue with the results from the overlap region.

In figures 3.5 and 3.6 the errors from the thick lenses are given as a function of the angle of the galvo. The errors are the outcoming angles in radians with respect to (parallels of) the optical axis.
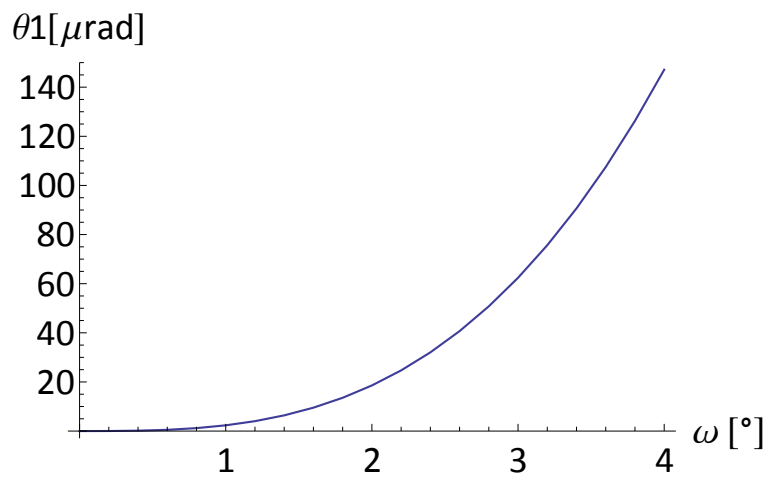
Figure 3.5: The deviation angle after the first lens with respect to (a parallel of) the optical axis as a function of ω_1.

The first figure 3.5 gives the deviation angle after the first galvo and is therefore a measure of the error at point F. The deviation angle at the mirror is given in figure 3.6 and is a measure of the error that can be detected at point P.
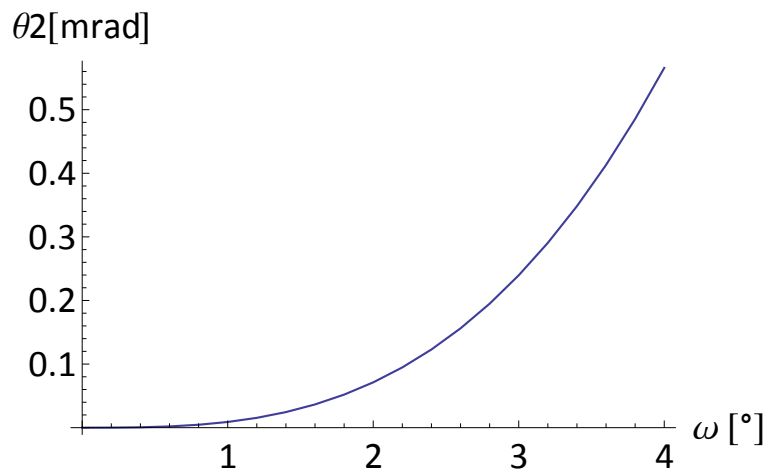

Figure 3.6: The deviation angle at second galvo with respect to the optical axis as a function of ω_1.

The overlap region of two beams with an angle respect to (a parallel of) the optical axis caused by the thick lenses is given in figure 3.7.
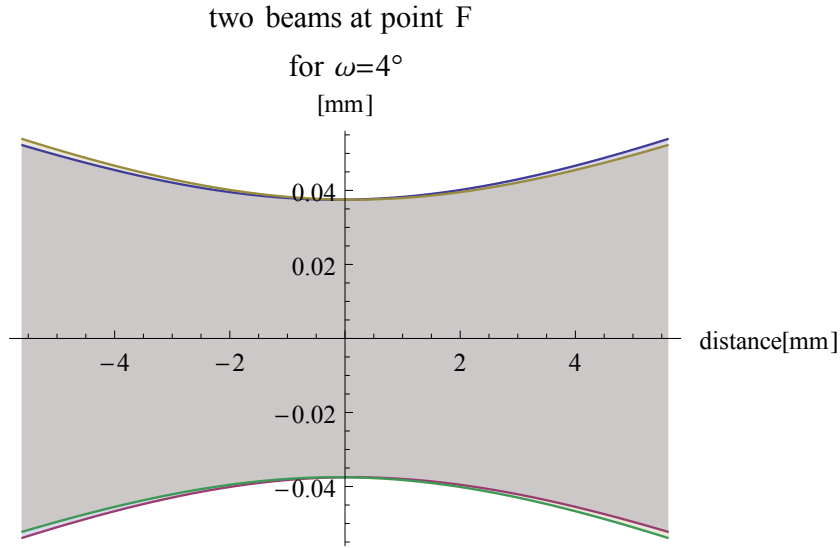
two beams at point F

for $\omega=4°$

[mm]

Figure 3.7: The overlap region of two overlapping beams for $z_R=5.6$ mm and $\omega_g=4°$.

The Rayleigh range of the optical lattice will be negligible smaller than the thin lens optical lattice and is $5.6 10^{-3}$m. Since the effect can be neglected, we can get the original desired optical lattice. As the outcoming angle of figure 3.5 is so small, $\cos\theta = 1$ can also be approximated really well. The lattice spacing of the standing wave will be $\lambda/2$ and is therefore not different from the lattice spacing with a thin lens.

Earlier we mentioned the third lens is placed to distinguish the unsynchronized error from the tick lens error.
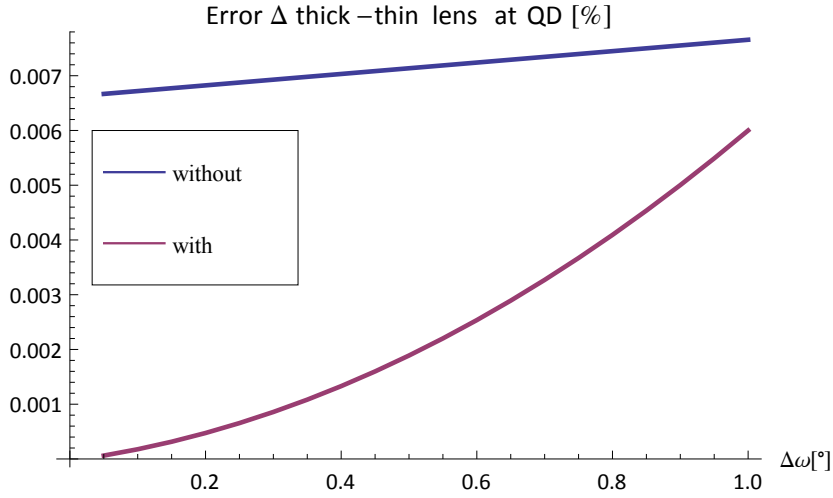
Figure 3.8: The error difference in percentage of the thick and with lens at the quadrant diode as a function of the angular difference between the first and second galvo. The angle of the first galvo was set at $\omega_1 = 4°$.

In figure 3.8 two curves are shown as a function of the angle difference between the two galvos. At first the error was calculated at the QD for the situation where the two lenses are thick lenses. Then the error was calculated for two thin lenses. By taking the percentual difference between both, we got the curves from figure 3.8. Now we consider the two different curves. The red curve represents the error difference with the thick third lens positioned in the setup. The blue curve represents the situation without this third thick lens.

From this figure we can conclude that with the third lens indeed there is a smaller difference between thick and thin lenses. This means the thick lens approaches the thin lens situation more accurately than without third lens. In the situation of thin lenses the beam propagates parallel to the incoming beam of the first galvo. To summarize, by capturing the error at the QD with the third lens we obtain only the error of the unsynchronized galvos.

3.2.3 Thin lens approximation

The calculations are compared with the approximation of the thin lens in figure 3.10. Especially at small ω_1 both calculations correspond accurately. In figure 3.10 b) only the intersection with the x-axis is different due to the deviation of the thick lens at a non-zero outcoming angle.
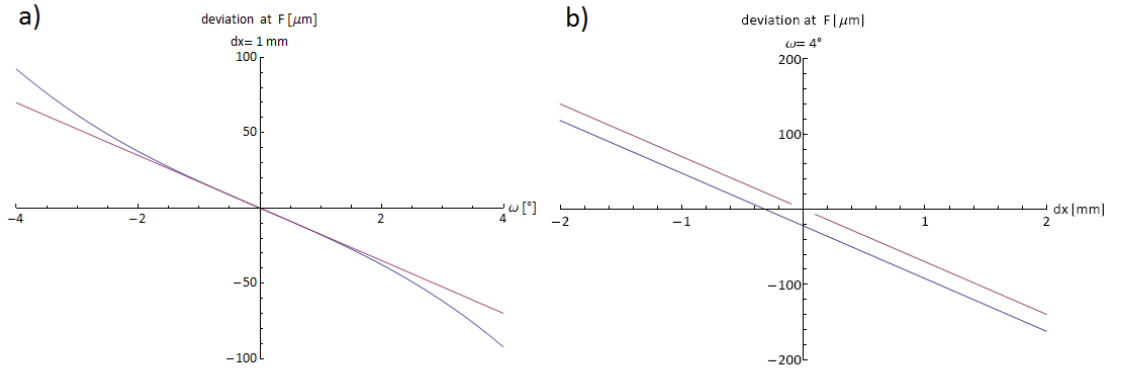
Figure 3.9: The deviations at the focus of the approximation of thin lens (purple) and thick lens calculation a)with varying outcoming angle and an offset on the first galvo of 1 mm. b) with varying offset at ω=4°.

To conclude this section, we can neglect the consequences of the small outcoming angle θ on both the lattice spacing and the overlap region. This means we can get the original desired optical lattice with a lattice spacing $\lambda/2$. The third lens can be used to approximate the errors with thin lenses, such that we will be able to capture only the error from unsynchronized glavo and mirror at point P.

3.3   Control System

To compensate for the above problems in alignment and possible noise and drift in the position at our scanning mirrors, we will implement a method to actively lock the position of one beam of the standing wave to the position of the other beam. We will now describe the control theory relevant to this work[28]. First linear feedback system will be introduced. In section 3.5.2 we will give an example of a controller. Next the so-called transfer function will give a mathematical representation of the system. In section 3.5.4 the system will be presented graphically with a block diagram. Section 3.5.5 will discuss the properties of system, such as the gain, zeros and poles. We will close this section with a so-called Nyquist Plot to represent the stability of the system.

A control system is a set of devices that manages the regulation of other devices. Because a linear feedback systems will be used, both linearity and feedback will be explained in the following paragraphs.

Linearity   A system is called linear when it satisfies the properties of superpositions and homogeneity. The principle of superposition tells us the response to the sum of two inputs, is the sum of the outputs corresponding to the individual inputs. A system is called homogeneous when a scaled input gives a similar scaled output.

Furthermore it should be mentioned that the system must be time-invariant, which means that after a timeshift on the input, the output will have the same timeshift.

Dynamics of a system can be represented by a differential equation. By using state variables, which give information about the past and predict the future, one can construct the state dynamics in state-space. The state-space is the set of values the process can take on and shows the behavior of the system. The state variables are collected in the state vector x and the output vector y.

For example a spring-mass-damper system can be represented by the differential equation $m\ddot{x} = F(t) - b\dot{x} - kx$, where $F(t)$ is the time-dependent exerted force, b the damping factor, k the spring constant and x the position of mass m. To determine the state-space representation, the second order differential equation must be reduced to a set of two first order differential equations. The position and velocity of the mass are chosen to be the state

variables $[\mathbf{x}] = \begin{bmatrix} x \\ \dot{x} \end{bmatrix}$. We then find

$$[\dot{\mathbf{x}}] = \begin{bmatrix} \dot{x} \\ \ddot{x} \end{bmatrix} = \begin{bmatrix} 0 & 1 \\ -\frac{k}{m} & -\frac{b}{m} \end{bmatrix} \begin{bmatrix} x \\ \dot{x} \end{bmatrix} + \begin{bmatrix} 0 \\ \frac{1}{m} \end{bmatrix} F(t) \tag{3.10}$$

$$y = \begin{bmatrix} 1 & 0 \end{bmatrix} \begin{bmatrix} x \\ \dot{x} \end{bmatrix} \tag{3.11}$$

For a first order linear state-space system the state-space equation can be generalized to

$$\begin{aligned} \frac{dx}{dt} &= Ax + Bu \\ y &= Cx + Du, \end{aligned} \tag{3.12}$$

where A, B, C and D are matrices and u is the added control vector. This general description of a linear system is really useful for the transfer function which will be introduced in section 3.5.3.

Feedback and Feedforward Feedback and feedforward terms will both be used in the setup of the test experiment. Therefore a general definition will be provided on such systems.
A feedback system is a process in which information about the past influences the same phenomenon in the present. Feedback systems react on disturbances by coupling the output signal back to the system. The purpose of these systems is to keep the *output* close to the *reference*, also called the *setpoint*.

Feedback systems can be split into two categories: positive and negative feedback systems. Negative feedback systems have an output that goes in opposite direction to the manipulated value and has a stabilizing effect.
Positive feedback however makes an increase in the input lead to an increase in the output. This mechanism is not stable and thereby not very common.
Feedforward systems correct in advance for a disturbance that is predictable. When this external disturbance is measured before influencing the system, a control signal can be implemented to counteract this. This control signal is called the feedforward control signal u_{ff}.

3.3.1 PID-controller

One of the most commonly applied negative feedback systems is a PID-controller[30].
A PID-controller is a controller device that consists of three different parts; a proportional (P), an integrator (I) and a differential (D) part. The purpose of the device is to minimize the error between the output of

the system and a reference signal. The *reference* signal or *setpoint* is the desired output signal of the system. With a PID-controller the output of the system will reach the reference signal in steady-state.

The output of the controller $u(t)$ is completely dependent on the input of the signal $e(t)$. The PID-controller can be described as a linear function as with three components.
The relation between the input and output of an ideal PID-controller with error feedback will therefore be

$$u(t) = k_p e + k_i \int_0^t e(\tau)d\tau + k_d \frac{de}{dt} = k_p(e + \frac{1}{T_i} \int_0^t e(\tau)d\tau + T_d \frac{de}{dt}). \quad (3.13)$$

This equation contains the three different parts of the feedback mechanism, corresponding to the so-called proportional, integrator and differential parts. They all have their own gain constants respectively k_p, k_i and k_d. The integral and differential gain constants k_i and k_d are often replaced by time constant $T_i = k_p/k_i$ and $T_d = k_d/k_p$.

The proportional part produces an output value proportional to the current error value. The constants of the system are analogue to constants in other fields in physics as fluids dynamics or mechanics. When considering for example a mechanical system, the proportional constant can be called the spring constant k in the equations of motion $F = m\ddot{x} = kx$, where F is the external force given to the system and x the position. A system with only a proportional part will therefore always oscillate around the setpoint, the higher the gain, the faster the oscillation frequency. In practice, as there will always be an undesired phase lag in the system at high frequency, a purely proportional system will oscillate when the gain is too high. Besides the technical problem, a purely proportional controller is not practical as the system will always oscillate with an amplitude proportional to the initial error. One should therefore at least add some damping. The derivative part produces an output value that is proportional to the time-derivative of the error. It therefore predicts the behaviour of the system. The derivative damps the possible overshoot and makes the system more stable. By drawing an parallel with mechanical system, the derivative constant is called damping factor b, which is proportional to the speed. When adding this derivative factor to our proportional system, we find the equation of motion $F = kx - b\dot{x}$.
When such a system reaches its steady-state under the condition that the set point changes as a function of time there will always remain an error.
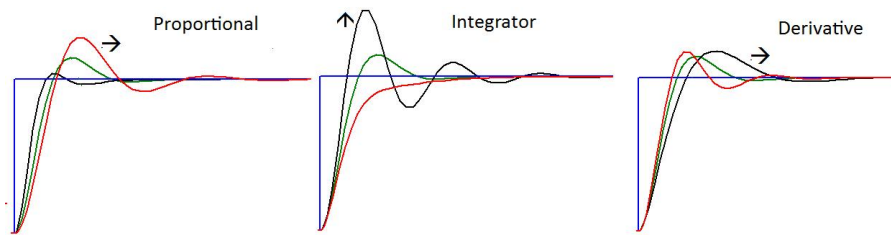
Figure 3.10: The output of a system with a PID-controller given an input of unit step function. The arrow gives the direction of change of the output when increasing the respectively proportional, integrator and derivative part of the controller.

By adding an integrator part this steady-state error can be eliminated. This integrative term accelerates movements of the process towards the reference by looking at the position in the past. A high integrative term will produce overshoot, because it corrects for errors from the past even when the error is also corrected for.

Since the process is disturbed and introduces phaselags, this PID-controller will be implemented to make the system reliable. In the following section the concepts of the representation of the systems and their properties are introduced to get more understanding of the controller and the relevant system.

3.3.2 Transfer function

A transfer function provides a representation of all kinds of linear feedback systems and describes its input/output relation. Mathematically the transfer function is the ratio of the Laplace transformations of the output and input under the assumption that all initial values are zero.

Laplace transform The Laplace transform $\mathcal{L}$ is a transform of a function f(t) from the time-domain to a function the frequency-domain. $\mathcal{L}(f(t))$ is the linear operator of function $f(t)$ to a function $F(s)$ depending on complex argument s. It is thus a generalization of the Fourier transform.

The Laplace transform is defined as

$$F(s) = \mathcal{L}(f(t))(s) = \int_0^\infty e^{-st} f(t)dt, \tag{3.14}$$

where $s = \sigma + i\omega$ with σ and ω being real numbers.

Another even faster way to get the transfer function is $G(s) = C(sI - A)^{-1}B + D$ where A,B,C and D are the matrices from Equation (3.12). We will give an example by finding the transfer function of a PID-controller.

29

The input and output of the controller is given by Equation (3.13). The Laplace transform of the output becomes

$$F(s) = \mathcal{L}(u(t))(s) = \int_0^\infty e^{-st}(k_p(e(t) + \frac{1}{T_i}\int_0^t e(\tau)d\tau + T_d\frac{de}{dt}). \qquad (3.15)$$

Solving this equation will give us $F(s) = [k_p + \frac{k_i}{s} + k_d s]e(s)$ and therefore results in

$$C(s) = k_p + \frac{k_i}{s} + k_d s, \qquad (3.16)$$

where $C(s)$ is the transfer function of the PID-controller.
Thanks to the simple building of this transfer function, the transfer function of a PI-controller can easily be found. Since this controller does not include a derivative part, the transfer function changes to

$$C(s) = k_p + \frac{k_i}{s}, \qquad (3.17)$$

The building of a system's transfer function from its components is straightforward[28]. This is demonstrated by using a so-called block diagram.

Block Diagram

The common way of representing the transfer functions of a system is a block diagram as figure 4.10. The diagram consists of three different parts; a process P, a controller C and a feedback -1. The process is pre-existing and consists of all parts of the system that are not influenced by the system. Different signals are shown with the following definitions: e is the error signal, r the reference, u the control signal and y the output signal. Possible disturbances to the process are represented in the figure as d.

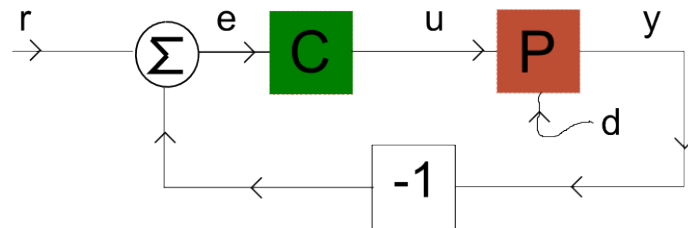Figure 3.11: The Block diagram of a general system with feedback and external disturbance d. It contains the unaffected process P and controller C. Besides it consists of reset r, error signal e, control signal u and output y.

This block diagram is an easy tool to find the total transfer function and represent the total system[28]. The feedback system with the controller and process of figure 4.10 has transfer function

$$G(s) = \frac{P(c)C(s)}{1 + P(s)C(s)}. \tag{3.18}$$

3.3.3 Properties System

In this section we want to find a controller that compensates undesired properties of the process. From the transfer function one can derive important properties of the system. Three important features are the gain and the locations of poles and zeros of the system. These properties give the necessary insight in the stability of the system.

The gain of the system represents the relationship between the magnitude of the output and input. The *zero frequency gain* is given the magnitude of the transfer function at s=0. This gain represents the ratio of the steady-state value of the output with respect to the input. Shortly this zero frequency gain is

$$G(0) = \frac{y_0}{u_0} = \frac{b_m}{a_n}, \tag{3.19}$$

where input stepfunction u is characterized by $u = e^{st}$ with s=0. There holds $a_n y_0 = b_m u_0$ with input u and output y and a_n and b_m are polynomials.

A transfer function can also be represented as

$$G(s) = \frac{b(s)}{a(s)}. \tag{3.20}$$

Several values of s give the transfer function (3.20) interesting outcomes. Those points are the zeros and poles of the system[31].

The frequencies giving zero output at a non-zero input are called the *zeros* of the system. For input $u(t) = e^{st}$ and $a(s) \neq 0$, the output will be $y = G(s)e^{st}$, which means the pure exponential output is zero if $b(s) = 0$. Shortly, the zeros can be found by taking the roots of $b(s)$ of Equation (3.20).

The *poles* of the transfer function represent the frequencies where the system has infinite gain. A system with infinite gain is impossible and will result in instability. We recognize this point as being the resonant frequencies of the system and must therefore be avoided. The infinite gain is produced when denominator $a(s)$ of Equation (3.20) is zero. When defining point p as a pole, one finds that $y(t) = e^{pt}$ is a solution of the differential equation with u=0.

A common representation of the properties of the transfer function is the Bode plot.

31

Bode Plot

The Bode plot is a graph of the transfer function of a system as a function of the frequency. Usually the bode plot is split into a Bode magnitude and the Bode phase plot. They express respectively the magnitude of the frequency response gain and the frequency response phase shift.

The frequency response of a linear function can easily be found from the transfer function with $s = i\omega$. The input will correspond to the complex exponential

$$u(t) = e^{i\omega t} = \cos \omega t + i \sin \omega t. \tag{3.21}$$

The output will result in

$$\begin{aligned} y(t) &= G(i\omega)e^{i\omega t} = Me^{i(\omega t + \phi)} \\ &= M\cos(\omega t + \phi) + iM\sin(\omega t + \phi), \end{aligned} \tag{3.22}$$

where M and ϕ are the gain and the phase of G,

$$M = |\, G(i\omega) \,| \tag{3.23a}$$

$$\phi = \arctan \frac{\mathrm{Im}(\mathrm{G}(i\omega))}{\mathrm{Re}(\mathrm{G}(i\omega))}. \tag{3.23b}$$

The characteristics of the system are determined by the poles and zeros and therefore characterize the plot as well. The corresponding frequencies of those points are called *frequency corners*. A simple example will clarify the Bode Plot in figure 3.12.
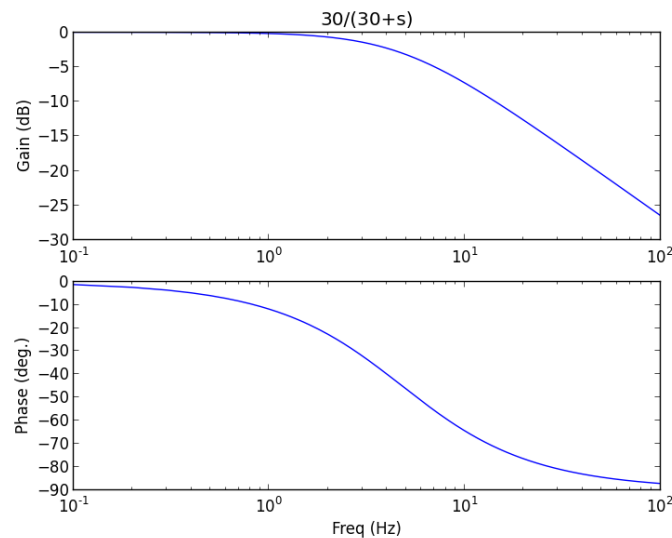

Figure 3.12: The Bode plot for function G(s)=a/(a+s) with a=30.

32

This bode plot is describing the first order transfer function $G(s) = a/(a+s)$ where $a = 30s^{-1}$. For this function the pole is positioned at s=-30, which corresponds to a frequency of $f = 4.8$ Hz. This pole is recognizable in the plot as a frequency corner.

The gain of this system is 1 until it reaches the frequency corner. At higher frequencies the gain goes to zero. This is essentially a low pass filter of first order.

Stability

One of the most important properties of a system is its stability. A linear system is called asymptotically stable only if all components in the homogeneous response decay to zero as time increases. The system is unstable when parts of the response diverge, which results in an oscillating output with a constant or increasing amplitude. The output oscillates with constant amplitude when it reaches the critical point. At this point the system has a phase of 180°, which would result in a positive feedback. The system is considered to be unstable when at the critical frequency the gain $M > 1$. The Nyquist plot makes it easy to tell if a system is stable or not.

Nyquist Plot

A Nyquist plot represents the real part of the transfer functions on the x-axis and the imaginary part on the y-axis as a function of ω. The transfer function of a open loop system with $s = i\omega$ gives the Nyquist curve in the diagram. The stability of the open loop system, which is the system without feedback will be investigated. If the open loop system is stable, the closed system will be stable as well.

Each frequency ω gives one point on the Nyquist plot and has a certain phase and gain. The phase ϕ is represented by the angle with respect to the zero frequency point. The gain M is the shortest distance between the point and the origin. An example of a Nyquist plot can be found in figure 3.13.
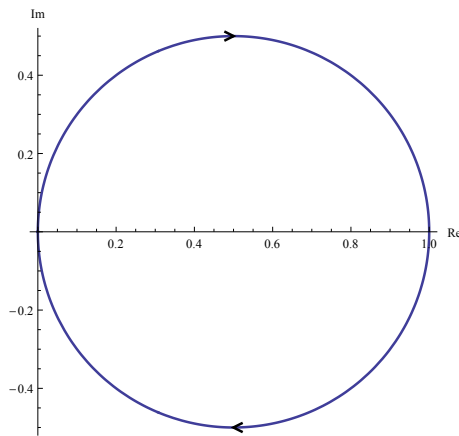
Figure 3.13: The Nyquist plot with the Nyquist curve of transfer function $G(s) = 30/(30 + s)$ for s=[-∞,∞].

Nyquist stability criterion   The absolute stability of a system is formulated by the following Nyquist stability criterion.

Any clockwise encirclements of the −1 *point by the open loop frequency response would indicate that the feedback control system would be destabilizing if the loop were closed.* One could summarize this, if the critical point is lower than −1, the first order linear system is unstable. The critical point corresponds to the point at critical frequency f_c with critical gain k_c. As the phase of the system is shifted to π, this point intersects with the negative x-axis in the Nyquist plot. The −1 point is the pole of the closed loop system; at this frequency the gain will go to infinity and must therefore be avoided. An example of an unstable system is given in figure 3.14 with corresponding Bode Plot 3.15.
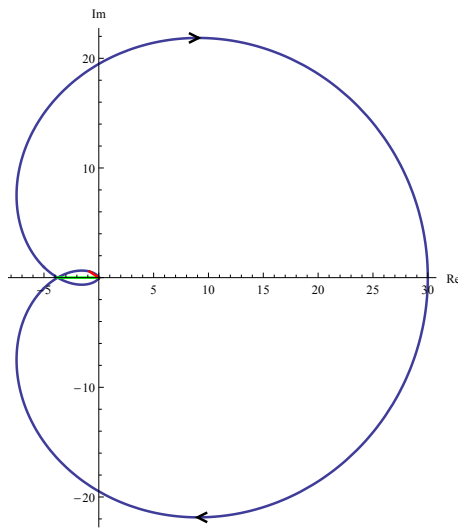
Figure 3.14: The Nyquist plot with the Nyquist curve of transfer function $G(s) = 30/(s+1)^3$ for s=[-∞,∞]. According to Nyquist's criterion this system is unstable, because it encircles the −1 point.
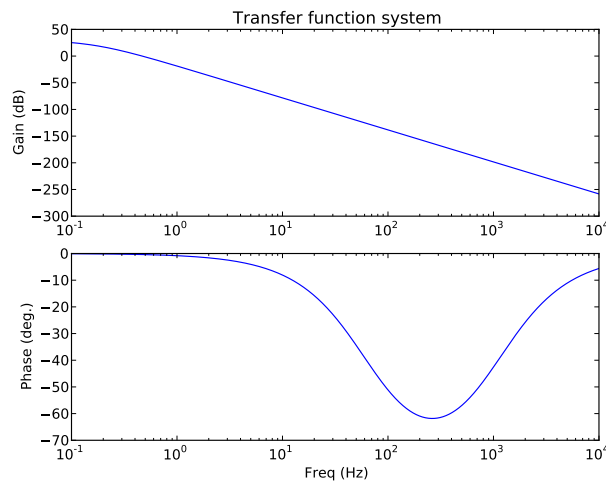

Figure 3.15: The Bode plot of transfer function $G(s) = 30/(s+1)^3$ for s=[-∞,∞].

Relative Stability   Measures of the stability of the system are the gain margin and the phase margin.

The *gain margin* is the inverse of the critical gain k_c, also called the ultimate gain k_u,($k_u = \frac{1}{k_c}$). On the Nyquist plot it is the amount of frequency response needed to move the critical point to the −1 point. This quantity gives the range of gain in which one can vary the gain of the system to still
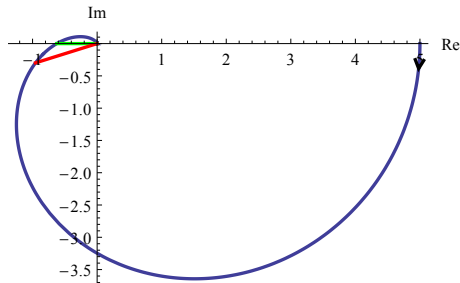
keep a stable system. This quantity is given in dB.

Figure 3.16: The Nyquist plot with the Nyquist curve of transfer function $G(s) = 5/(s+1)^3$ for s=[0,∞]. The −1 point is not encircled, so the system is stable. The green line gives the gain margin, while the phase margin is given by the red line.

The *phase margin* is the angle that the frequency response would have to change to move the critical point to the −1 point. This quantity gives us the range of phase in which we can play with the constants to hold the system stable.

<div style="text-align: right;">*4*</div>

Scanner

The purpose of the test experiment of the scanner is building a working
1D-scanner with one pair of galvos. This chapter discusses the properties
and problems around the two galvos.

The first problem will be discussed in section 4.2 and the second problem in
section 4.3. A final test experiment in section 4.4 will test our 1D-scanner.
First the galvo will be introduced with some general information.

4.1 The Galvo

Four Galvo Mirror Systems will eventually move the atoms in 2 dimensions.
Each system consists of a mirror mounted on the axis of a motor and the
electronics to control the motor. The bandwidth of the system is kept
below 1kHz to avoid electromechanical resonant. The atoms will be moved
approximately in 0.1 s over a range of 1 cm which demands the galvo to
move with a frequency of approximately 10 Hz.

In figure 4.1a) the relation is shown between the angle of the galvo and the
resulting movement. This displacement is calculated at the focal distance
from the first achromat; exactly in between both achromatic lenses. Since
the lenses are achromats an error is introduced at this focal distance and
is given in figure 4.1b). This error comes from the deviation in outcoming
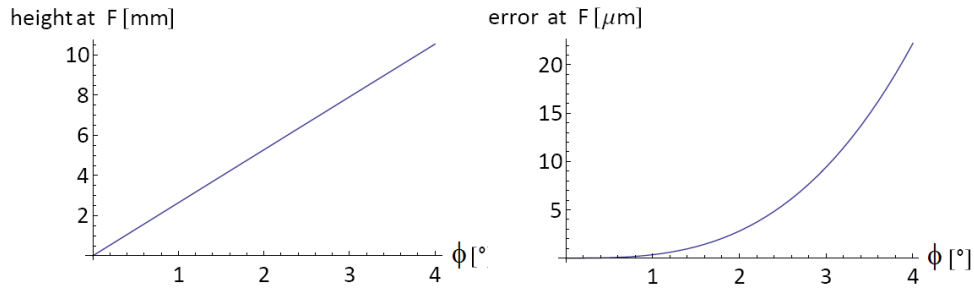angle of the thick lens.

Figure 4.1: a) The height of the beam with respect to the optical axis at the focus of the first lens as a function of the angle of the galvo. b)The error of the beam at the focus of the first achromat as a function of the angle of the first galvo. The error is a result of a small outcoming angle from the achromat with respect to the parallel of the optical axis.

The electronics of this galvo consist of a mirror assembly and a driver card. The mirror assembly is composed of the motor and a protected silver-coated mirror.

The driver card controls the motor of the mirror and has a diagnostic terminal output that can return certain quantities from the motor. The test experiment uses the position, the positional error and the motor coil terminal of the galvo. Those terminals are connected to a National Instrument Card (USB-6211) that can read those different quantities and other outputs from devices such as a quadrant diode (QD).

The NI-card is connected to a laptop, on which a python script runs with a few varying parameters. Those parameters are the driving function, frequency, amplitude, number of oscillations, samples per oscillation and the offset.

4.1.1   The Servo Driver Board

The Servo Driver Board Schematic Diagram in figure 4.2 shows the feedback mechanism of the galvo.

This servo is a class 0 servo, where the 0 indicates the number of integrators. The lack of integrators makes this system a PD-controller, but an extra differentiator part was added, which will be explained in the following section.
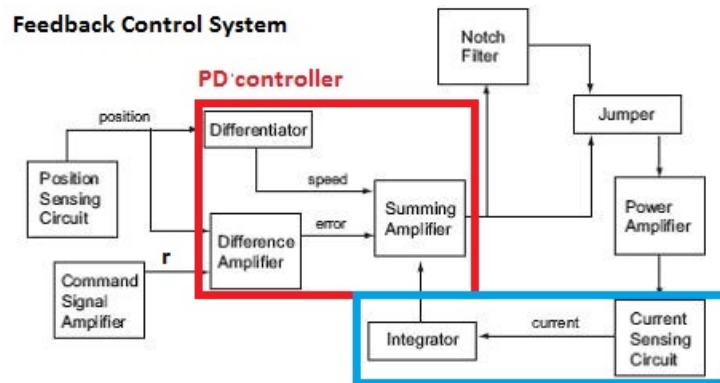
Figure 4.2: The Servo Driver Board Diagram with the PD-controller in the red box. The blue box consists of the parts to get the second derivative part for compensating the lag.

The diagram of figure 4.2 shows the control components.

Set point The position sensing circuit calculates the position of the galvo. To calculate the speed, the differentiator takes the derivative of the position. This speed dams the overshoot of the output signal and could therefore be called the D-part of the controller.
The difference amplifier calculates the error from the set point and position. This is the proportional part of the PD-controller. The summing amplifier takes care of the correcting signal of the PD-controller reaching the setpoint.

Lag The mirror of the galvo is positioned by a motor that is managed by a coil current. This current induces a torque and thus an acceleration. The drive electronics however are controlled by the coil voltage. Due to the inductive nature of the motor a lag between the voltage and current will occur. The inductive reactance of the motor is caused by the changing magnetic field which in turn is caused by changing current. This lagging causes an overshoot of the position of the galvo.
In other words, when the controller reaches the setpoint, it takes time before the current will react, which causes an overshoot in position. This overshoot needs to be damped by an extra derivative term.
Fortunately the driver board consists of another part that will take care of this lag. The current sensor in the diagram measures the acceleration of the motor. The integrator integrates the acceleration to the speed which is fed into the controller to damp the overshoot.
The lagging of the current and voltages causes a decrease in power as well, which is compensated by the power amplifier.

Resonance At last, this system stores and transfers energy which results in resonance at a certain frequency. To avoid this resonant frequency the notch filter is installed. The Notch filter is a band-stop filter with a narrow stop band. The remaining part that needs some explanation is a jumper, which is a short length conductor that closes an electrical circuit.

4.2 Servobump

To summarize, the lagging of the current with respect to the voltage discussed in the previous section, causes a position overshoot. Oscillations are damped at small values of this lagging. As we saw before, if the lag is more than 180°, the systems' output starts to oscillate with increasing amplitude.

When a beam is reflected by a stationary galvo on the QD, the position of the beam is measured. The position of the beam on the QD should thus not move, any motion is caused by noise in the angle of the galvo. When converting this noise into a fourier noise spectrum, a so-called servobump becomes visible around 1.5 kHz.
The high noise amplitudes of the position of the galvo will result in a high frequency oscillating optical trap as well. As this is around twice the trap frequency of the atoms in the scanner this can cause rapid heating. This servobump was observed in previous tests[24] and is our first concern of working with galvos.

By tuning the internal parameters of the controller of the galvos we will minimize this servobump.
From previous sections we conclude that if we want the overshoot to disappear, there are two things we can adjust. First the proportional part can be decreased to make the galvo slower. By making the galvo slower, it will be easier for the motor to follow the movement so the lag will be smaller. The decrease in speed will results in a larger reaction time for the system, which will decrease the overshoot. Secondly the derivative part can be increased to make the dampening factor higher. The tuning procedure will be explained in the following section.

4.2.1 Setup and Method

To tune the galvos and minimize the servobump we used the setup of figure 4.3.
The setup consists of several parts; a QD, an achromatic lens and a galvo, that are aligned as in Appendix B 'aligning setup'. The quadrant diode is connected to the NI-card as described before. To get rid of the
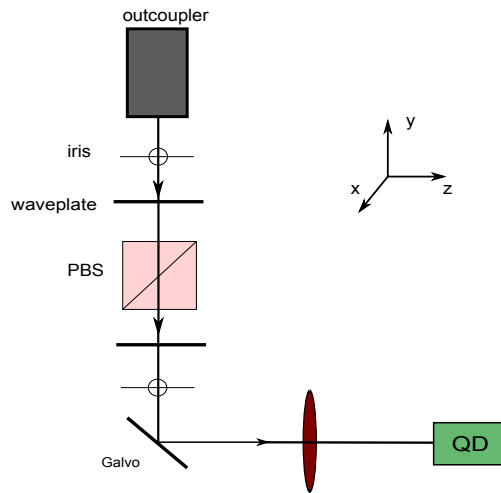
Figure 4.3: The top view of the setup of tuning galvo.

servo bump, the internal PD-controller of the galvo is adjusted with different potentiometers on the board. One of the difficult things of the knobs is that they are really closely related, which makes it impossible to adjust only one of the parameters.

4.2.2 Results

After making the system slower and reducing the overshoot, the outputs of the three terminals changed significantly. In figure 4.4,4.5, 4.6 and 4.7 the different quantities of the galvos are presented before and after tuning.
The motor coil current is decreased after tuning, since the acceleration of the mirror is smaller when producing a slower movement. In the position measurement we observe an increasing settling time and no overshoot, thanks to the lower proportional constant and the higher damping factor. Since the system becomes slower, the position error has a higher settling time.
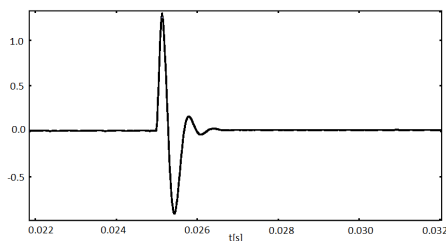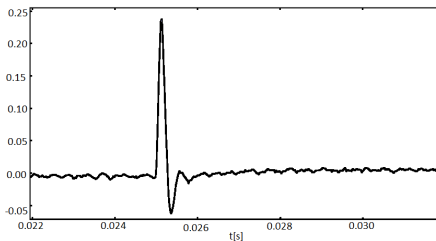

Figure 4.4: The motor coil current before tuning

Figure 4.5: The motor coil current after tuning
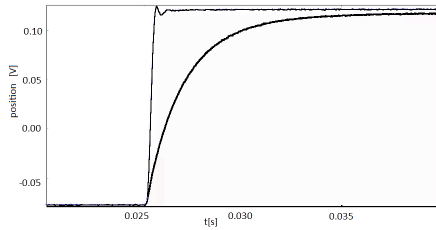
41

Figure 4.6: Position before and after (thick line) tuning
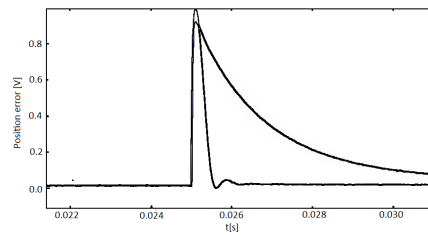

Figure 4.7: Position error before and after(thick line) tuning

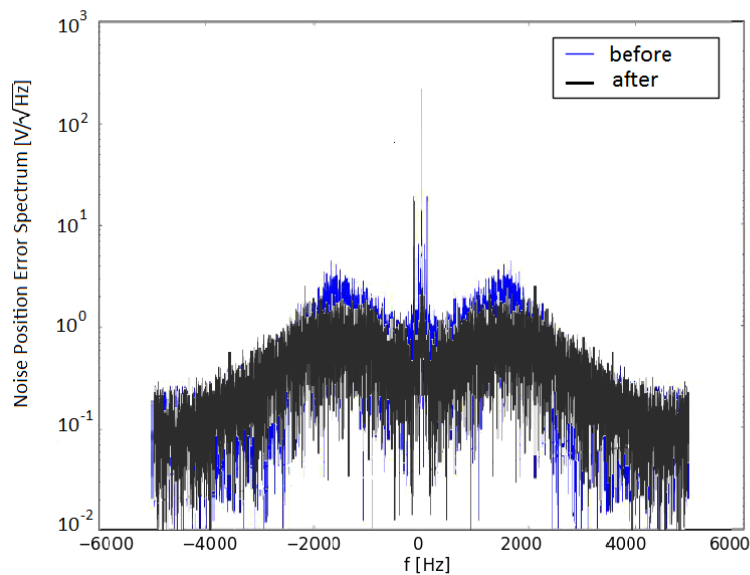In figure 4.8 the fourier spectrum of the position is shown before and after tuning the galvo.

Figure 4.8: The noise spectrum of Galvo 2 before and after tuning

First the ratio between the top of the bumps and the band becomes smaller and the spectrum looks a lot smoother. Secondly the low frequency oscillations became smaller after tuning except from the zero point. On the wings the values are a bit higher, but overall we can see the noise level has been decreased. This means we reached the goal of decreasing the servo bump by a factor of around 5.

To conclude, by tuning the galvos the noise fluctuates less around 1.5 kHz, so the servo bump became flatter. At the wings, the oscillations look a bit higher than before tuning.

42

4.3 PI-controller

The next step to construct a well working scanner is installing a PI-controller in our system.

4.3.1 Setup and System

Let us introduce the system we will use to actually move the beam at the focus in one dimension. The test setup contains two galvos and three achromats, as in section 3.4. The setup of figure 4.9 differs from figure 3.3 by the starting point and the mirror which are replaced by galvos. The QD replaces point P and measures the error signal.
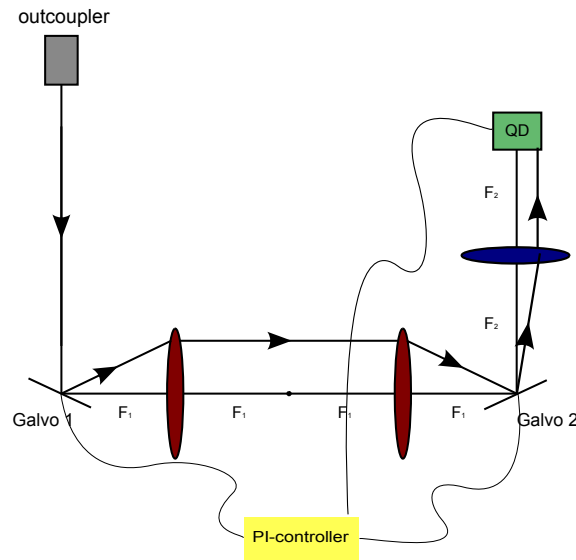

Figure 4.9: The top view of the setup eliminating the error at the QD. It consists of the outcoupler with an outcoming beam, three (two red and one blue) achromats, the two galvos, the Quadrant Diode and the PI-controller. The controller is connected electronically to both galvos and the QD.

In the experiment the two beams must overlap to create a standing wave and trap the atoms. The beams must remain perfectly overlapped also when the galvos are scanning. The deviation at the position of the QD is a measure of this overlap. Since we do not want to change the overlap region between the two lenses, only the error from the unsynchronized galvos should be minimized at the QD. Remind, the third lens takes care of taking only the desired error and the PI-controller minimizes this error. The PI-controller will position the second galvo at the same angle as the

first galvo, where $\omega_1 = \omega_2$. Ideally the beam propagating after hitting the second galvo will propagate parallel to the beam coming from the outcoupler and will cause no error at the QD. However we use achromats and have alignment errors, which result in errors at the QD. The PI-controller will take care of the error from unsynchronized galvos at the QD. The derivative part of the PID-controller is not necessary since the controller is adequate for a first order system[28].

The PI-controller consists of two inputs and one output. One input is the error signal from the QD which will be minimized. The second input is the feed forward term, which is the driving signal of the first galvo. The output of the controller is the driving signal of the second galvo. The driving signals will move the galvos to the desired angles respectively ω_1 and ω_2.
By changing the angle of the first galvo, the beam will move a certain distance at the focus of the achromats. A reminder, this is the distance the atoms will move and is discussed in section 4.1. Finally the PI-controller must be stable which requires insights in the gain constants of the controller.

Block diagram We will fit our setup into the general block diagram of figure 4.10. The pre-existing process P(s) contains the QD and the second galvo and are uneffected by changes in this system. The C(s) is the controller in the system, which is in our case the PI-controller. The reference signal r is always set to zero, since the errorsignal should approach zero. The system symmetry therefore results in $e = -y$, with y being the output signal.
The driving signal of the first galvo is a known external disturbance for which should be corrected. Since this disturbance is know, it can be added to the system as a feedforward term u_{ff}. The feedforward term is always added to the control signal u to correct before the disturbance is added to the process..

Since we want to obtain the general block diagram, the disturbance term is made as a function of the feed forward term. Actually the driving signal of the first galvo is a real big (known) disturbance, so this is justified.
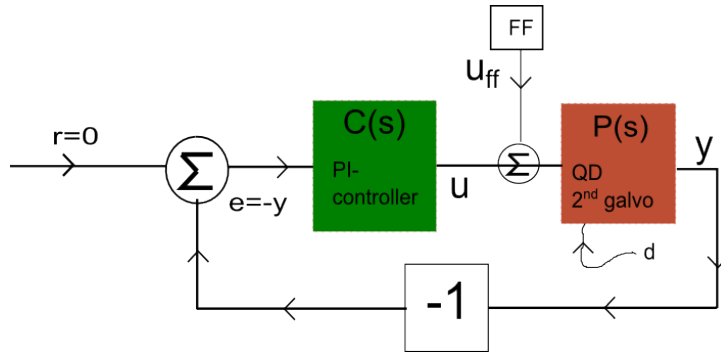
Figure 4.10: The Block diagram of a general system with feedback, feedforward term u_{ff} and external disturbance d. It contains the unaffected process P and controller C. Besides it consists of reset r, error signal e, control signal u and output y.
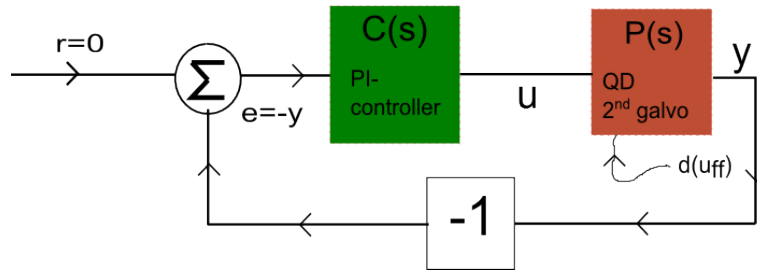

Figure 4.11: The block diagram of the system with a process, a controller and a disturbance which is caused by the first galvo. By using feed forward, the process already takes care of this disturbance before it occurs. The feedback loop gives the output back to the input to eliminate the error.

The transfer function of this linear feedback system can thus be formed by the general transfer function of the block diagram $G(s) = \frac{P(s)C(s)}{1+P(s)C(s)}$. In the following section we will discuss the transfer function of the process in more detail. The transfer function of controller (3.17) will give the total system transfer function

$$G(s) = \frac{P(s)(k_p + k_i/s)}{1 + P(s)(k_p + k_i/s)}. \tag{4.1}$$

From the Nyquist criterion the condition for a stable system is known $G(i\omega_c)_o > -1$. When considering the system at critical frequency, it is open looped and only has the proportional part of the controller. An open loop function does not contain feedback, which results in a transfer function given by $G(i\omega_c)_o = P(i\omega_c)C(i\omega_c) = M_P e^{i\theta} M_C$, where M_P and M_C are respectively the gains of the process and the controller. θ is the phase of the process and will be discussed in more detail in the

following section. At the critical frequency the phase difference between both components is π. At critical frequency only the proportional part of the controller is used, which is independent of the frequency. This results in the open loop transfer function at critical frequency $G(i\omega_c) = -k_c k_p$.

Concluding, if we want the system to be stable, one should satisfy $k_p < \frac{1}{k_c}$.

4.3.2 Determining Constants

Before fabricating the PI-controller, the resistance range of the potentiometers on the board of the controller should be estimated.

Figure 4.12 shows the schematic technical display of the PI-controller, which consists of two resistors R_1 and R_2 and a capacitor C_2. Both resistors are related to both the proportional part and the integrator part, while the capacitor contributes to only the integrative part.
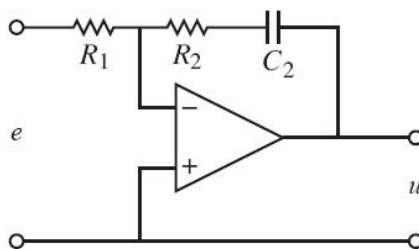

Figure 4.12: The schematic display of a PI-controller containing an optical amplifier, two resistors and a capacitor. The input is given by e and the controller output by u.

To find the relation between the gain constants and the resistors we will look at the transfer functions of the system. The transfer function of the controller as a function of the gain constants is given in Equation (3.17). The transfer function of the controller in figure 4.12 can also be given by the ratio of impedance $\frac{-z_2}{z_1}$, where $z_1 = \frac{R_1}{1+sR_1}$ and $z_2 = R_2 + \frac{1}{C_2 s}$. Those equations give the transfer function of $C_s = \frac{R_2}{R_1} + \frac{1}{sC_2 R_1}$ which should be equal to the transfer function (3.17). This results in the relations of the gain constants and the resistors,

$$k_p = R_2/R_1, \tag{4.2a}$$

$$k_i = \frac{1}{C_2 R_1}. \tag{4.2b}$$

46

To summarize, the equations will give us the ranges of the resistors in the controller. Therefore we first need values for the gain constants.

Ziegler-Nichols' tuning rules The Ziegler-Nichols' tuning rules give those estimation values for the gain constants of PI(D)-controllers. It already includes the restrictions of the system to become stable. Thereby it matches the system response at zero and critical frequencies and the rest is fixed in between. With a simple experiment on the system together with the tuning rule, one can derive the parameters for the controller.

The tuning rules are based on assumptions that the process is a first order linear system. The process should be stable, non-oscillatory and approximated by a first-order lag characteristic. The first order lag characteristic means that the unit step response resembles an s-shaped curve without overshoot; the step response has a slope and approaches asymptotically the reference value.
Earlier the transfer function of the process was simplified to $Me^{i\theta}$ with a gain and a phase, now the actual standard form will be presented. The transfer function of a first order process has the form

$$P(s) = \frac{Ke^{-sT_1}}{1 + sT_2}, \tag{4.3}$$

where K is defined as the zero frequency gain, T_1 and T_2 as timeconstants. T_2 contains the phase lag of the system till $\pi/2$, while the remaining lag is represented by the exponent with T_1. They are defined by the fact that at critical frequency the phase is π. $T_1 = (\pi - \phi)/\omega_c$, $T_2 = \frac{1}{\omega_c}\sqrt{K^2 k_c^2 - 1}$ and $\phi = \arctan \omega_c T_2$. Both constants can be obtained from the measurements of the process.

To be able to analyse the complete system two measurements were done to find the critical frequency and the zero frequency gain. We found a critical frequency of $f_c = 1600Hz$. At this frequency the critical constant is $56 \ s^{-1}$. Zero frequency gain $K = 100$ is approximated by the gain at low frequency.

The Ziegler-Nichols' tuning rules in the *frequency response method* applies a unit step input to the process and records the response. We used the more empirically improved tuning rules[28]

$$k_p = 0.22k_c - \frac{0.07}{K} \tag{4.4}$$

and

$$k_i = 0.16k_c f_c + \frac{0.62f_c}{K}. \tag{4.5}$$

With the improved tuning equations the proportional constant has been calculated to be around k_p=0.0043 s^{-1} and the integration constant around k_i=6.5 s^{-1}. This results in a value range for resistor R_1 from 0-200 kΩ and R_2 from 0-5 kΩ. Those potentiometers were installed in the system to get a working PI-controller.

Implementing the potentiometers gives us the technical design of the PI-controller, which is shown in Appendix D 'Design PI-controller'.

4.3.3 Optimization

To optimize the PI-controller we will use the 'compensating' setup of figure 4.9.
The testing and tuning is done with a driving signal of

$$x(t) = \frac{A}{2} + \frac{A}{2} \sin{(2\pi f t - \pi/2)}, \tag{4.6}$$

where A is the maximum distance the beam moves at the focus, f the frequency and x the position at the focus perpendicular to the optical axis as a function of time.

On the board represented in figure D.1 different pods were installed to optimize the PI-controller. The parameters of the pods are called, the *tau*, the *HFgain* and the *gain*. The *tau* tunes the first resistor (R1 of figure D.1), while the *HFgain* adjusts the second resistor (R2 of figure D.1). The *gain* potentiometer manipulates the constant amplification of the incoming signal, which should be adjusted such that the reference and output signals are of the same magnitude. There is also a switch to turn off the integrator part of the PI-controller. The next step is to adjust the parameters to get a minimal oscillation at the QD.

4.3.4 Results

After optimizing, the PI-controller the error signal with and without PI-controller was measured. Without the PI-controller the second galvo is controlled purely by the feed forward and thus receives the same driving signal as the first galvo. Figure 4.13 represents the output of the PI-loop and the driving signal of the first galvo. As we expect the signals look very similar.
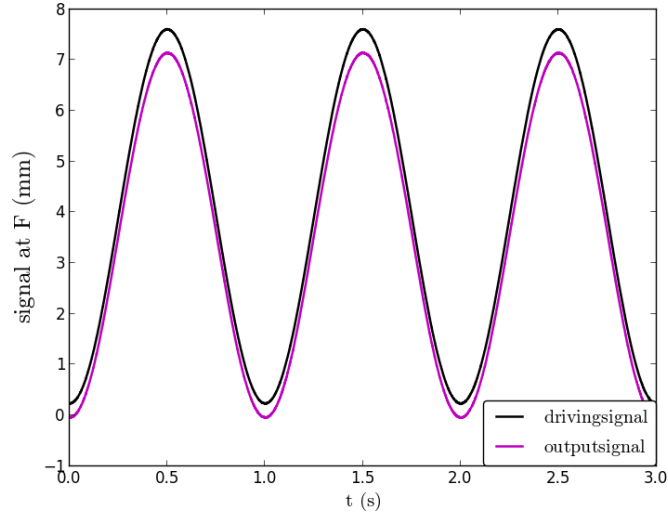
Figure 4.13: Both the driving signal of the first galvo and the output signal of the PI-controller (which will be the drivingsignal of the second galvo) driven with a translation distance A of 7.5 mm at the focus of the first lens.

In figure 4.14 and 4.15 the error signal is shown with and without the PI-controller for different amplitudes. By connecting the PI-controller the error signal on the QD was decreased substantially.

For a 1.1 mm translation of the beam at the focus the error amplitude was lowered from 20 μm to a RMS-value of the noise signal of 0.93 μm; the oscillation becomes invisible.

For a 7.5 mm translation the error amplitude was flattened at 45 μm. This is because the QD saturates for those large errors. After switching on the PI-controller, the RMS-value becomes 0.91 μm, when subtracting the oscillation.
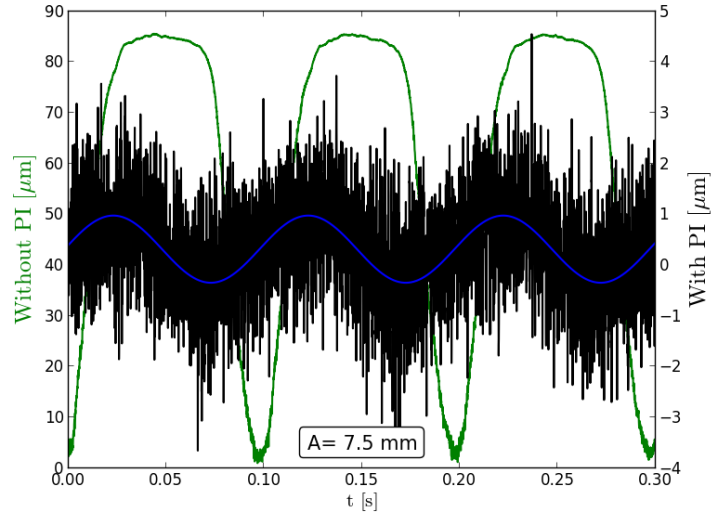
Figure 4.15: The Error signal with (black) and without (green) the PI-controller with a translation distance of 7.5mm at the focus. The blue line gives the fit of the signal with PI-controller and has an amplitude of 0.67 µm. The RMS-value is 0.92 µm.
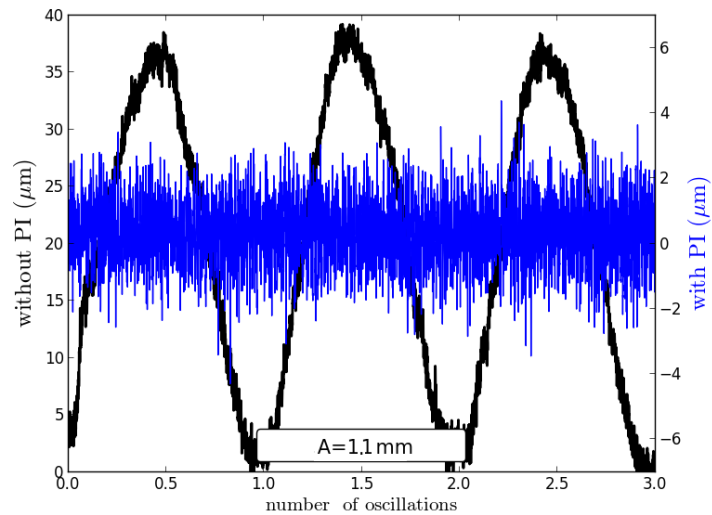

Figure 4.14: The error signal with and without the PI-controller with a translation distance of 1.1 mm. With PI the RMS-value becomes 0.93 µm.

Thanks to the switch, we are able to compare the results with and without the integrator. One of these plots is represented in figure 4.16 from

which we can conclude that a the proportional part decreased the error with a factor of two, while the remaining error was minimized by the integrator.
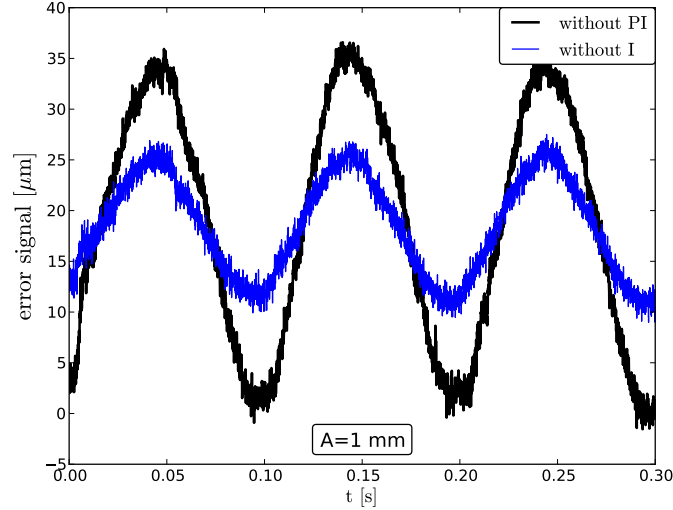

Figure 4.16: The error signal without PI-controller and without the integrator of the controller with a translation distance of 1.1 mm.

After these measurements, the proportional and integration constants are calculated and measured to compare with the designing values.
To get the proportional constant, the integration part of the PI-controller was switched off. The ratio of the driving signal and the output signal of the controller without the integrator, gave the right proportional gain constant. The integration gain constant was harder to get, because one can't switch off the proportional part of the controller. By measuring the voltages at TP5 and R24 of figure D.1 and using Ohm's law, the values of the resistors were calculated.

The calculated values of the gain constants are k_p=0.0012 s^{-1}(vs. design 0.0043 s^{-1}) and k_i=7.9 s^{-1}(vs. design 6.5 s^{-1}).
The values of the gain constants are in the same order as the design values and within the range of the resistor, which means the PI-controller has been designed well. The parameters of the transfer function of the process are T_1=2.2 10^{-4}s and T_2=1.5 10^{-4}s and $K = 100$ s^{-1} in Equation (4.3). The transfer function of the process becomes

$$P(s) = \frac{100e^{-2.210^{-4}s}}{1 - 1.510^{-4}s}. \tag{4.7}$$

The critical gain k_c is 56 s^{-1} and the gain margin k_u from relation

$k_u = \frac{1}{k_c}$ becomes 0.018 s^{-1}. To recall this gain margin gives the amount of gain that could be adjusted to the system until it gets unstable.

k_p is lower than k_u, thus we can confirm we have a stable system.

Finally we checked the noise spectra with and without the controller. From figure 4.17 we conclude the controller has no influence on the noise spectrum, which is logical given the small bandwidth of the controller.
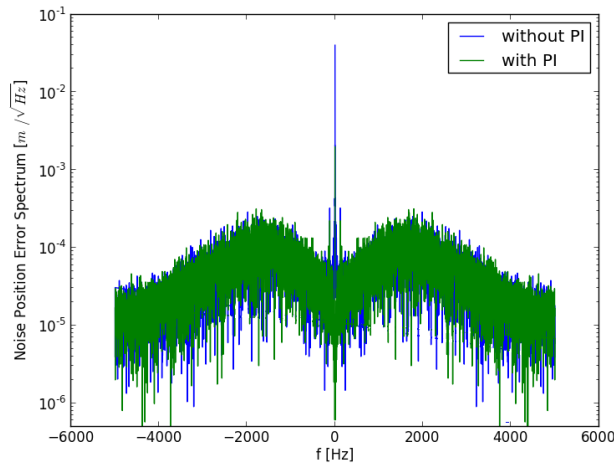

Figure 4.17: The noise position spectrum with and without the PI-controller connected to the setup.

4.4 Scanner test

This 1D-scanner has been tested by coupling light that is reflected over both galvos back into a single mode fiber. A working feedback system should remain coupled in the fiber even when the mirrors are scanning.

4.4.1 Setup

The setup of this final test experiment looks similar to the setup of the PI-controller discussed in section 4.2. A beam pick-off and incoupler have been added. The QD has been replaced by an incoupler and after the outcoupler a powermeter is installed to measure the power of the light coupled into the second fiber. The amount of light coupled into the fiber is dependent on the position and angle of the incoming light beam. The setup is shown in figure 4.18. The powermeter is connected to the NI-card and the laptop to analyse the obtained results. Two mirrors are added to walk the beam into the fiber.
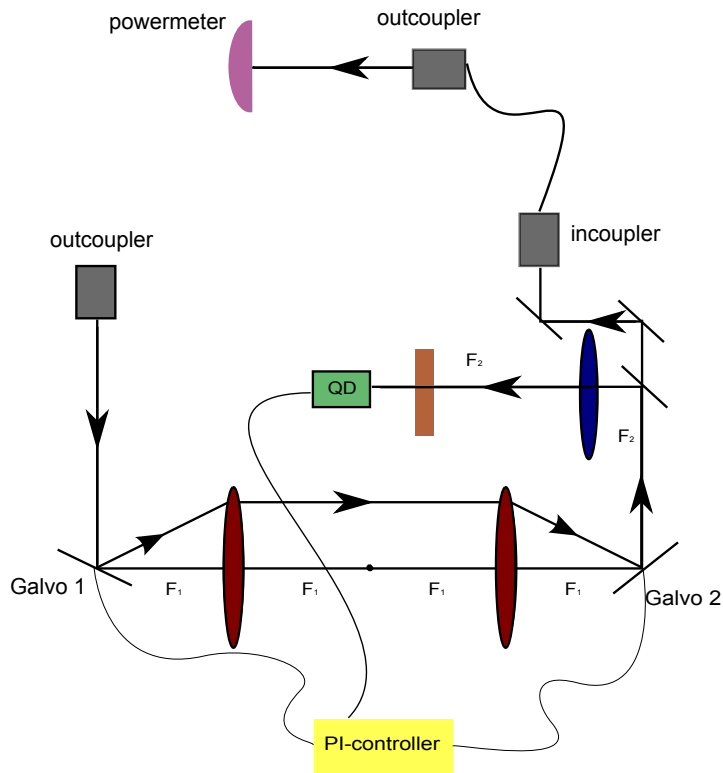
Figure 4.18: The powermeter setup for the last check of the scanner: if it possible to couple the light into the fiber while the galvos are scanning. Same distances are chosen as in the setup of section 4.2, the incoupler is placed at a distance of 284 mm from the second galvo.

The PI-controller uses the error signal of the QD after a beam pick-off. Also a neutral density-filter is placed to obtain the correct intensity of light at the QD.

Adding the controller in the setup results in the second galvo getting the same angle as the first galvo; $\omega_1 = \omega_2$. This setup results in a minimum error at the QD without changing the overlap region when introducing a counter propagating beam. Remember, when $\omega_1 \neq \omega_2$ a counter propagating beam would have another path than the first beam. This would influence the overlap region of both beams at the focus of lenses, which we do not want.

4.4.2 Method

The first galvo is moved with the shifted sine function of $\frac{A}{2} + \frac{A}{2}\sin 2\pi ft$. To recall, A is the total deviation at the focus between both lenses. The powermeter gives the amount of light that is coupled into the second fiber. First we assume all light coming out from the fiber will be measured by the power meter. Secondly we assume the light intensity at the powermeter is linear dependent on the error at the incoupler.
The setup was optimized by changing the position and lenses and tuning the PI-controller.

The PI-controller was tuned by minimizing the error signal the QD and maximizing the parameter. By changing the *tau* and *HF-gain* knobs of the PI-controller, the proportional and integrative constants were changed.

4.4.3 Results

After optimizing we measured the error signal at the QD and the power at the powermeter. The measurements will be discussed in the following sections, after which the experiments will be concluded in chapter 5.
Since we optimized the PI-controller in the newest situation, the gain constants of the controller changed as well to k_p=0.0021 and k_i=22.6. Those values will result in the final system represented in the last paragraph.

Error signal

We measured error signals of figure 4.19, with and without the P(I)-controller with a translation distance of 7.5 mm at the focus.
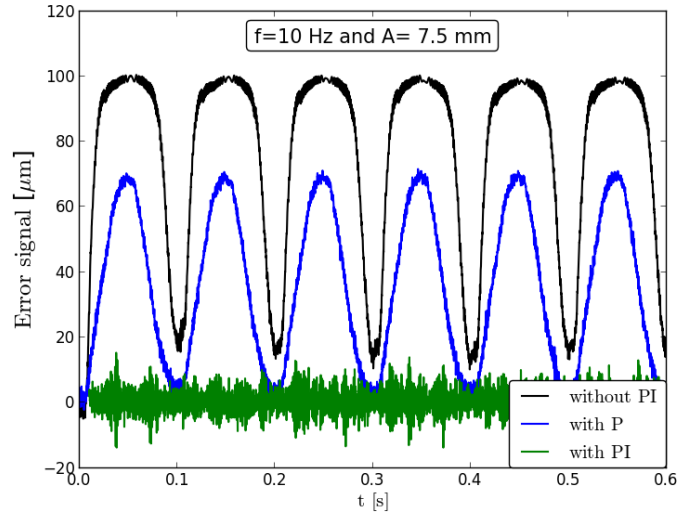
Figure 4.19: The errorsignal at the QD with and without P(I)-controller. The translation distance A at the focus is 7.5 mm with a frequency of 10 Hz. With PI-controller the RMS-value becomes 3.68 μm.

The error signal with the PI-controller is in the same order of magnitude as the error signal without any oscillations of the galvos, which can be seen in figure 4.20. The RMS-value of the noise is 3.7 μm with respect to the 1.6 μm of the noise with a flat signal. Concluding, the PI-controller accurately decreases the error at the QD down to the noise level.
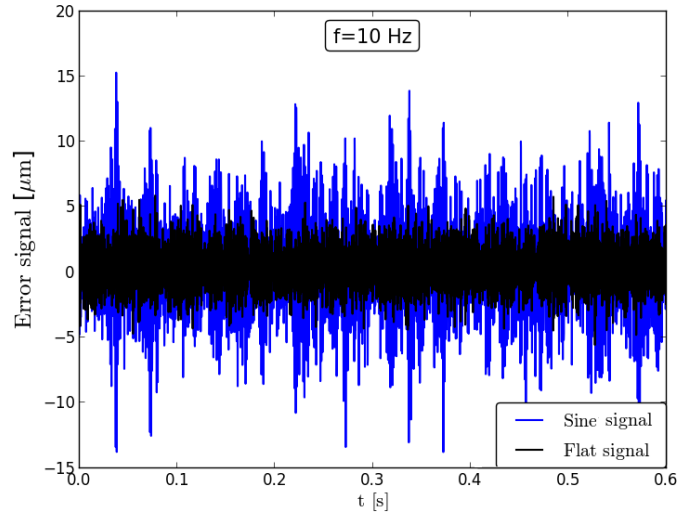
Figure 4.20: The errorsignal at the QD with PI with a driving function of zero or a sine function with translation distance of 7.5 mm at the focus with a frequency of 10 Hz. The RMS-value of the flat and sine signal are respectively 1.55 µm and 3.68 µm.

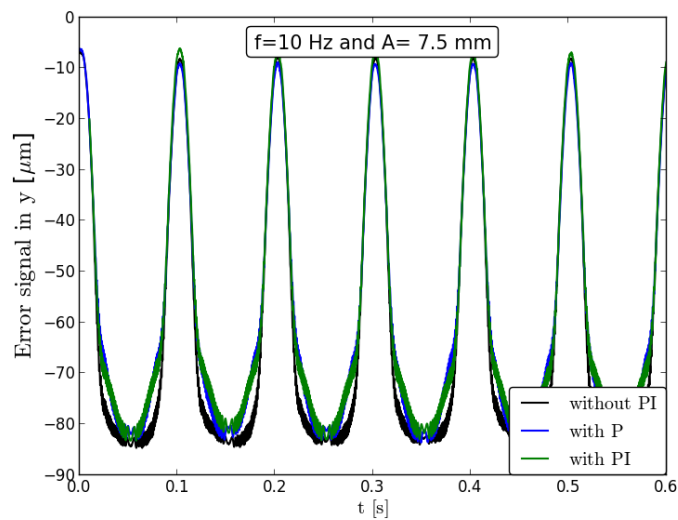In figure 4.21 the error signal in the y-direction is shown for the three conditions.

Figure 4.21: The errorsignal at the QD in y-direction for the three conditions with and without P(I)-controller. The RMS-value of the error with PI-controller is 29.2 µm.

In this figure there is barely a difference between the error with and without the controller. This shows that the PI-controller has, as expected no influence on the y-oscillations.

Since the y-oscillations have the same frequency as the galvo, the origin of this y-oscillation seems to be the galvo. Most probably the rotating axis of the galvos are not standing perfectly perpendicular to the plane which the beam is reflected on then. A slight angle of the galvo will therefore result in a visible offset in the y-direction at large distances.

Since the errors at the QD in x- and y- direction can be calculated from the calculation of section 3.4, the error at the incoupler can be estimated as well and is represented in table 4.1.

Angle galvos [°]	translation distance [mm]	Direction	Error RMS at QD [μm]	Error RMS at incoupler [μm]
2.8	7.5			
		x	3.68	15.36
		y	29.3	47.40
1.4	3.75			
		x	3.45	6.77
		y	24.43	39.52
0.4	1.1			
		x	2.86	4.66
		y	13.67	22.12

Table 4.1: The errors at the incoupler according to the thick lens calculations by using the detected errors at the QD. Actually only the case of 0.4 degrees is reliable, since at the QD this errorsignal was the only signal not to be saturated.

The RMS values of the errors at the QD are translated back to the outcoming angle θ of the second galvo. The x- and y-directed errors differ at one point; the galvo does not rotate in the same plane as the y-directed errors. Therefore we assume the beam hits the second galvo at the center for errors in the y-direction. The point where the beam hits the second galvo in the x-direction is calculated by taking the corresponding angles of the two galvos (first column of table 4.1). Since we use the PI-controller those angles are identical for the two galvos. The total error in the x-direction consists of the error from the outcoming angle θ and the distance from where the beam hits the galvo to the center of the galvo.Since both the outcoming angle as this distance have big values in the case of an angel of 2.8 degrees of the galvos, the total error at the incoupler will be a lot higher than the errors at smaller angles.

Actually only the case of 0.4 degrees is reliable since it is the only case where the error signal was not saturated. This will result in even higher values for

larger angles and probably more similar ratios between x- and y- errors to the case of 0.4 degrees. From the table we can conclude the y-directed errors dominate the total error at the incoupler with a factor around 5.

Powermeter signal

The signal from the powermeter is shown as a function of time in figure 4.23, 4.22 and 4.24.
As a result of the (calculated) errors in x- and y- direction at the incoupler, the power fluctuates as a function of time.
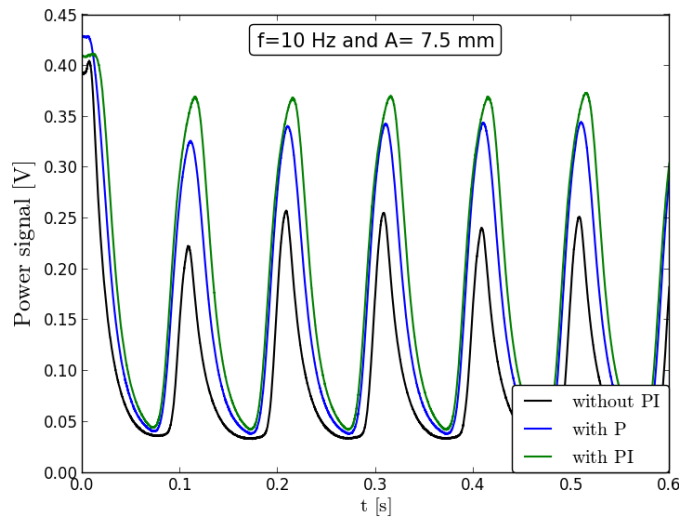

Figure 4.22: The power as a function of time with a translation distance of 7.50 mm and a frequency of 10 Hz for three different conditions.

From the figures a mean, an amplitude and a phase lag (when comparing it with the condition without controller) are found. Those parameters will be discussed after some explanation.
Since the drive function starts at zero, the *mean* value of the power is around $A/2$. The *amplitude* of the output oscillation is dependent on the total errors at the incoupler. From the previous section we know those errors are dominated by errors in the y-direction.
At t=0 s of figure 4.22 the amount of incoupled light is maximum, as the alignment was done with zero input signal to both galvos.
The last parameter is the *phase lag*, which depends on the reaction time of the PI-controller. The parameters are given in table 4.2 and will be discussed in the following parts.

	Mean(V)		Amplitude(V)		Phase(rad)	
Drive function	with P	with PI	with P	with PI	with P	with PI
A7.5 f5	0.20	0.23	0.17	0.20	0.10	0.0063
A7.5 f10	0.19	0.21	0.16	0.17	0.18	0.47
A3.75 f20	0.22	0.27	0.10	0.10	0.28	0.72

Table 4.2: Values from data of the powermeter at different conditions, where A is the amplitudes and f the frequency.
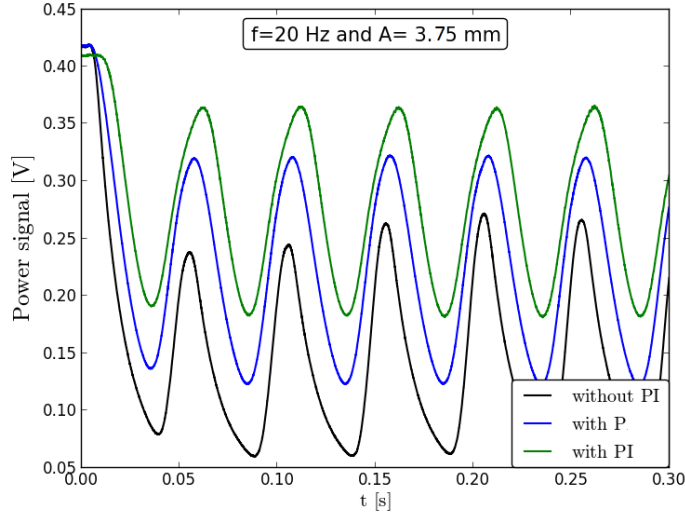

Figure 4.23: The power as a function of time with translation distance at the focus A of 3.75 mm and a frequency of 20 Hz for three different conditions.

In the three graphs of figures 4.22, 4.23 and 4.24, the error in the y-directions is represented, since this error dominates the signal. When looking at the values of the maxima of, those values without PI-controller are unstable. Since the maximum values are stable with the PI-controller, the system with this device is ameliorated.

The mean increases at the condition with PI-controller. As expected the PI-controller decreases the outcoming angle (with respect to the optical axis) of the second galvo by eliminating the error from the unsynchronized galvos, which results in a smaller error at the incoupler and thus a higher mean value.

The lower amplitude case of figure 4.23 has a higher value of the mean as well, because of the smaller amplitude from the galvos.
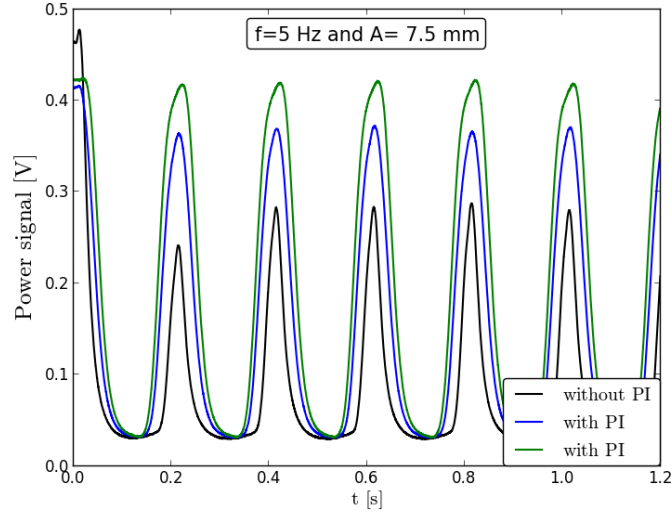
Figure 4.24: The power signal measured at the power meter. The translation distance is kept the same as in figure 4.22: 7.5 mm at the focus and the frequency is 5 Hz for three conditions. The parameter reaches almost 1.

The amplitude at a translation of 7.5 mm and a frequency of 5 Hz of figure 4.24 almost doubles with the PI-controller. Since the angle of the galvo is twice as big, we indeed expect the error amplitude to be two times bigger. When nevertheless looking at the same amplitude at higher frequency (f= 10Hz), the output seems to have a harder time in following the drivingsignal.

During the optimization of the PI-controller we wanted the ratio of the first two maxima to increase to reach a maximum beam incoupling. At low frequency (figure 4.24) when the PI-controller is added, the output follows the input closely thus the ratio goes to 1. Adding the controller increases the ratio in all cases. The higher the frequency, the more the system damps the output.

At last the phase lag between the outputs with respect to the case without controller is discussed. As we expect, adding the P(I)-controller increases the lagging. An increase in lagging is found at increased frequency. At high frequency the lag in the controller becomes higher, so automatically lags the output of the system.

The fourier transform of the noise in this system is shown in figure 4.26. At 1.5 kHz the position error increases, since the controller amplifies noise. At lower frequency the noiselevel is lower than without the controller.
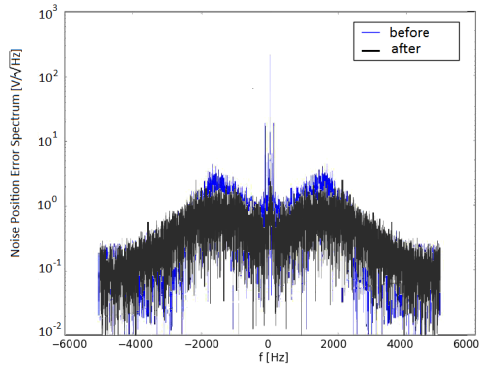
Figure 4.25: The fourier spectrum of the noise before and after tuning the servobump.
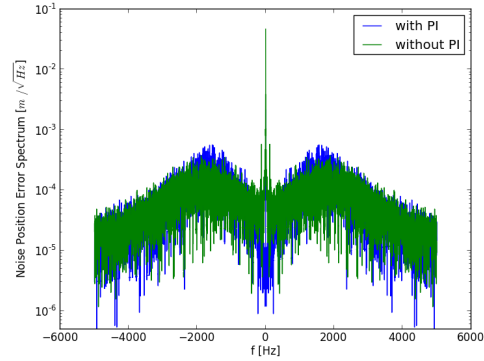

Figure 4.26: The fourier spectrum of the noise with and without the PI-controller.

System representation

This last section contains the representation of the final system.

Figure 4.28 and 4.27 show the open loop bode plots of the system respectively without and with integrator. In the curves of all four plots we observe a nod. This nod corresponds as expected to the frequency corner at the critical point at f=1600Hz. The curve drop results in a highly phased output with zero gain, which can be interpreted as a low-pass filter system. The difference between both plots is resulted by the integrator of the controller. This integrator introduces an extra factor of $\frac{\sqrt{(\omega/k_i)^2+1}}{\omega/k_i}$ in the magnitude plot and $\arctan \omega/k_i - 90°$ in the phase. For small frequencies this integrator results in a phase of a constant 90° and an extra gain magnitude term which results in the linear curve in logscale. Thanks to the decay term in the process transfer function, the phase goes to minus infinity and the magnitude to zero at high frequency.
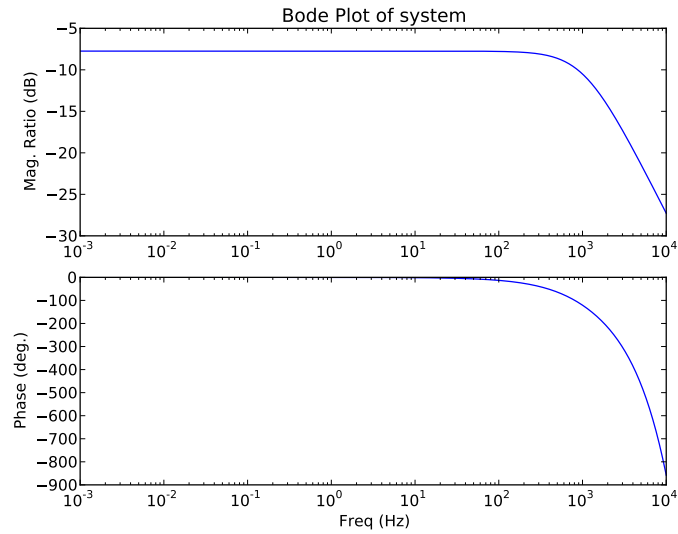
62

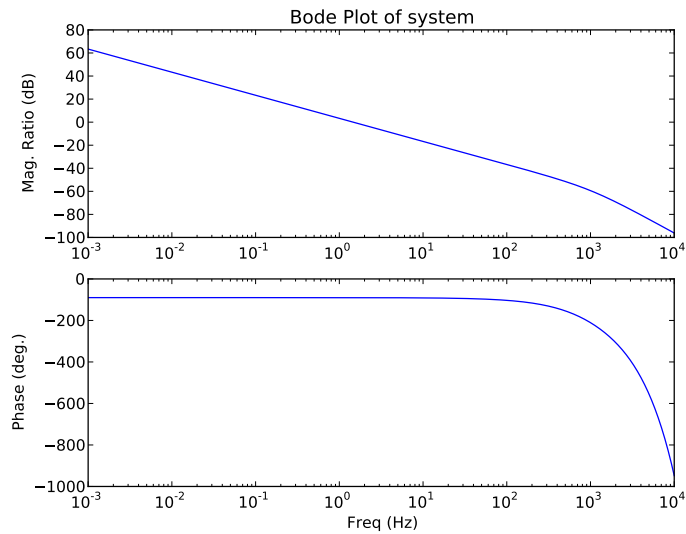*Figure 4.27: Bode Plot of the open loop system without integrator.*

Figure 4.28: Bode Plot of the open loop system with integrator.

Figure 4.29 shows the Nyquist plots of our open loop system consisting only the proportional part of the controller. The curve is traversing clockwise. The crossing of the curve with the negative real axis represents the critical point and corresponds to the value of the Bode Plot of this open loop function at the critical frequency.
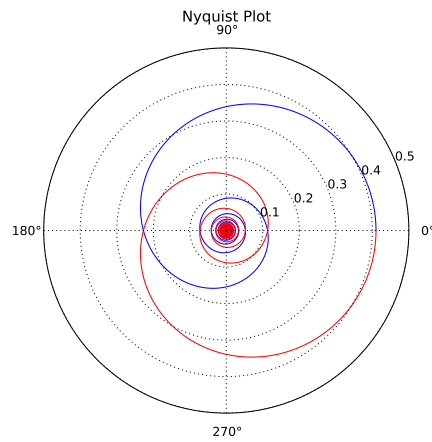
Figure 4.29: Nyquist Plot of the open loop system only with the proportional part of the controller with frequencies $[-\infty, \infty]$. Since the Nyquist curve does not encircle the -1 point, this system is stable. In red the positive frequencies are given, while the negative frequencies are shown in blue.

Figure 4.30 represents the Nyquist plot of the system with the integrator. Since the integrator introduces a pole at s=0, the Nyquist plot blows up at small frequencies. The lowest frequency value is chosen to be 250 Hz to get the right scale to show the encirclements of the curve. The dotted green line connects the negative and positive frequencies with a circle with a radius of infinity. Since the Nyquist curve does not encircle the -1point, this system is stable.
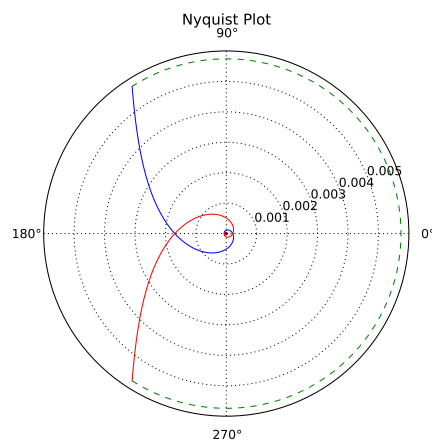

Figure 4.30: Nyquist Plot of the open loop system with the integrator for positive frequencies [250, 10^6 Hz] in red and negative frequencies [-10^6, -250Hz] in blue. This system is stable is well.

5

Conclusion

In this thesis the setup of a 1D-scanner has been tested. The two problems that arose during testing were solved to meet the requirements of the device. First of all the servobump needed to decrease to minimize heating of the optical trap. Secondly the two counter propagating beams had to overlap along the whole path.

The servobump of the galvos has been tuned by its separate internal controllers. The bump decreased significantly in the noise spectrum. It would be interesting to investigate how much the trap would heat when using galvos instead of mirrors. One could compare those results with the same experiment with not-tuned galvos to quantify the improvement in heating as a result of the tuning.

Secondly the overlap of the beams along the path was investigated. Consequently the achromatic lenses and the errors due to these lenses have been studied.
The achromatic lens introduces a deviation angle when a light ray goes trough this lens. However the overlap region of both counter propagating light beams is not influenced significantly by this introduced angle. This means it is still possible to construct the desired conveyor with those achromats.
The errors introduced by the achromatic lenses and misalignments are minimized by introducing a controller. By canceling the error of the beam at one defined point (at the QD), the overlap is maximized along the path of the beam. A PI-controller connected to the setup of the 1D-scanner was successfully designed and installed. The controller is able to reduce the error signal at the QD to noise level.
Finally the beam was coupled back into a fiber after which the intensity of the beam was measured with a powermeter. Even when oscillating both

galvos with the required angles of the experiment the powersignal was non-zero. This means it is possible to overlap beams when adding another counter propagating beam and moving both galvos.

The errors at a point after the two galvos and thus at the powermeter are found to be dominated by y-directed errors. Fortunately the scanner will be extended to two dimensions by adding two galvos. The errors in y-direction will theoretically be compensated by the other pair of galvos connected to a second PI-controller. This remains to be seen in further studies of the scanner.

In the future this 1D-scanner will be expanded to the designed 2D-scanner. It would be interesting to review the deviation in the y-direction of that system to examine the compensation of the deviation. However, unfortunately it seems not possible to measure the errors of the scanning movement at the focus.

Besides, the system can probably still be optimized by tuning the internal controllers of the galvos when connected to this system. When this 2D-scanner is indeed able to scan in two directions, we will implement it into the experiment. Then, the atoms will be moved above the nanostructure for the investigation on the interaction between light and matter.

6

Acknowledgements

A year in the nanophotonics group of Dries van Oosten has been a year full of new experiences and learning. I would like to thank Dries for his devotion to the experiment and giving me a place to develop. I'm glad I got this opportunity to take part of this "high risk high gain" experiment.

I would like to thank Sandy for his help during this whole year. The experiment asked sometimes a lot from our patience but it worked out, 'perfect' or not... Besides I want to thank Sebastiaan and Bas for working so hard on this project together with me and always be there with me in good and bad times. Of course Christiaan, Stephan, Tessa and Bruno were also really nice for some relaxation during lunchtime, thanks! At last I would like to thank my father Peter Kluit a lot for his support during the last phase of this research, the skype conversations and the feedback on my thesis. I hope this thesis has given some insights in the scanner and I hope in the end there a lot of interesting measurements on the interactions between atoms and surface plasmons will be done with many successful results!

Bibliography

[1] Kik P.G., Brongersma M.L., *Surface Plasmon Nanophotonics*, Springer Series in Optical Sciences **131**, 2007 p.1-9

[2] Wood R.W., *On a remarkable case of uneven distribution of light in a diffraction grating spectrum*, Phil.Mag. **4**, 396 (1902)

[3] Pines D., *Collective energy losses in solids*, Rev. Mod. Phys. **28**, 184-198 (1956)

[4] Pitarke J.M., Silkin V.M., Chulkov E.V. and Echenique P.M., *Theory of surface plasmons and surface-plasmons polaritons*, Rep.Prog.Phys. **70** 1-87 (2007).

[5] Ritchie R.H., *Plasma Losses by Fast Electron in Thin Films*, Phys. Rev. **106**, 874 (1957).

[6] Manson J.R., Ritchie R.H., *The Attractive Interaction Between an Atom and a Surface*, Nuclear Instruments and Methods in Physics Research **82**, 422-426 (1984).

[7] Powell C. J. and Swan J. B., *Origin of the Characteristic Electron Energy Losses in Aluminum*, Phys. Rev. **115** 869 (1959)

[8] Stern E. A. and Ferrell R. A., *Surface Plasma Oscillations of a Degenerate Electron Gas*, Phys. Rev. **120** 130 (1960)

[9] Barnes W.L., Dereux A. Ebbesen T.W. *Surface plasmon subwavelength optics*, Nature **424** (2003).

[10] Mandel O., Greiner M., Widera A., Rom T., Hnsch Th. W. and Bloch I., *Controlled collisions for multi-particle entanglement of optically trapped atoms*, Nature **425**, 937 (2003).

[11] Lezec H.J., Degiron A., Devaux E., Linke R.A., Martin-Moreno L., Garcia-Vidal F. J., and Ebbesen T. W., *Beaming light from a subwavelength aperture*, Science **297**, 820 (2002).

[12] Ebbesen T. W., Lezec H. J., Ghaemi H. F., Phio T. , and Wolff P. A., *Extraordinary optical transmission through sub-wavelength hole arrays*, Nature **391**, 667 (1998).

[13] van Coevorden D. V., Sprik R., Tip A., and Lagendijk A., *Photonic band structure of atomic lattices*, Phys. Rev. Lett. *77*, 2412 (1996)

[14] Reymond G., Schlosser N., Protsenko I. and Grangier P., *Single-atom manipulation in a microscopic dipole trap*, Phil. Trans. Roy. Soc. Lond. A **361**, 1527 (2003)

[15] Phillips W.D., Metcalf H.J., Sci. Amer. **36**, (1987) also see http://www.nobel.se/announcement-97/phyback97.html.

[16] Cohen-Tannoudji C.N., Phillips W.D., *New Mechanisms for Laser Cooling*, Physics Today, (1990), p.33-40

[17] van der Straten P., *Laser cooling and trapping*, New York, 1999.

[18] Muckley E.S., *Constructing a Magnetic Optical Trap for cold atom trapping*, California, 2009.

[19] Kuppens et al *Loading an optical dipole trap*, Phys. Rev. A **62**(2000) 013406.

[20] Grimm R., Weidemller M. *Optical Dipole Traps for Neutral Atoms*, Adv. At. Mol. Opt. Phys. **42**, 95 (2000) physics/9902072v1.

[21] Schmidt S., *Long distance transport of ultracold atoms using a 1D optical lattice*, New Journal of Physics **8** (2006) 159.

[22] Meschede D., Schrader D., Kuhr S., Alt W., M$\ddot{u}$ller M. and Gomer V., *An optical conveyor belt for single neutral atoms* Appl.Phys. B **73** 819-824 (2001)

[23] Alt W., Schrader D., Kuhr S., M$\ddot{u}$ller M., Gomer V., Meschede D., *Single atom in standing wave*, Phys. Rev. Lett. **67**,(2003)

[24] Kouyzer P., *Moving Cold Atoms* (2012)

[25] Verboven T., *Magneto-Optical Trap Optimization* (2013)

[26] Meyer Viol B.,*Optical Dipole trap for Rb-87 atoms*(in progress)

[27] Greveling S., *A Stereo-Tweezer for Ultra Cold Atoms* (in progress)

[28] Astrom K.J., Murray R.M., *Feedback Systems, An Introduction for Scientists and Engineers*, Princeton, 2008.

[29] Wolf E., Born M., *Principles of Optics*, Cambridge, 1999.

[30] *A Self-Testing PID Loop*, Microstar Laboratiories 1994-2009, *http://www.mstarlabs.com/control/selftest.html*

[31] *Analysis and Design of Feedback Control Systems, Understanding Poles and Zeros*, Massachusetts Institute of Technology, $http://web.mit.edu/2.14/www/Handouts/PoleZero.pdf$

[32] van Oosten D., *Quantum gases in optical lattices: the atomic Mott insulator*, Utrecht, 1975.

Front Focus

A.1   Focal Lengths

The achromatic lenses got three different focal lengths. A front focal, back focal and system focal distance. Those focal lengths have the following definitions. The back focal length is the length from the back surface of the lens till the focus, see figure A.1. The front focal length is the distance from the front surface to the point where the rays are focused.
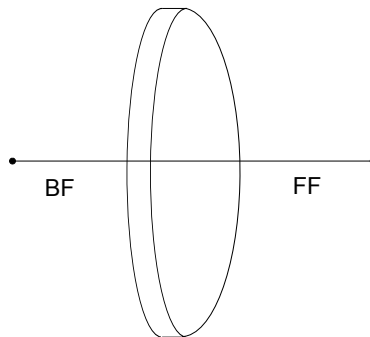

Figure A.1: An achromatic lens with its back and front focal length.

From the Thorlabs website one can get the back focal length, while the front focus has to be calculated. This was done by solving a few equations on ray optics one can find the back focal length of the lens. One assumption made is that if an parallel ray is hitting the back of the lens, it will focus in the back focal point.

Finding Front Focus   We start with the used Equations (A.1) and (A.2) to find the front focal length.

$$\begin{aligned} \alpha &= \arcsin \tfrac{y}{R_3} \\ \beta &= \arcsin \tfrac{y_2}{R_2} \\ \gamma &= \arcsin \tfrac{y_3}{R_3} \end{aligned} \tag{A.1}$$

$$\begin{aligned} \theta_{i1} &= \arcsin \tfrac{y}{R_3} \\ \theta_{r1} &= \arcsin \tfrac{\sin \theta_{i1}}{n_1} \\ \theta_{i2} &= \beta + \theta_{r1} - \theta_{i1} \\ \theta_{r2} &= \arcsin \sin \theta_{i1} \tfrac{n_2}{n_1} \\ \theta_{i3} &= \gamma + \beta - \theta_{r2} \\ \theta_{r3} &= \arcsin \sin \theta_{i2} n_3 \end{aligned} \tag{A.2}$$

By solving the equations mentioned below one gets the coordinates at which the ray of light hits the surfaces of the different parts in the achromatic lens, see figure A.2. All those equations are depended of the incoming height of the light ray.
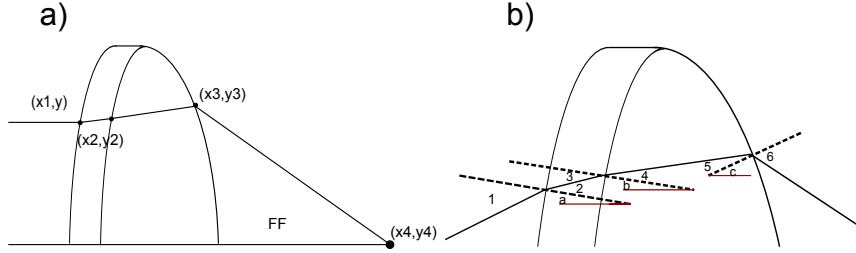

Figure A.2: Achromatic lens with a) coordinates and b) angles. 1. $= \theta_{i1}$, 2. $= \theta_{r1}$, 3. $= \theta_{i2}$, 4. $= \theta_{r2}$, 5. $= \theta_{i3}$, 6. $= \theta_{r3}$, $a = \alpha$,$b = \beta$, $c = \gamma$

$$x_1 = R_3 - \sqrt{R_3^2 - y_1^2} \tag{A.3}$$

$$y_2 = y - (x_2 - x_1)\tan\theta_{r1} - \theta_{i1} \tag{A.4a}$$
$$= \sqrt{R_2^2 - (R_2 - x_2 + t_{c1})^2} \tag{A.4b}$$

$$y_3 = y_2 - (x_3 - x_2)\tan\theta_{r2} - \beta \tag{A.5a}$$
$$= \sqrt{R_1^2 - (R_1 + x_3 - t_c)^2} \tag{A.5b}$$

$$y_4 = y_3 - (x_4 - x_3)\tan\theta_{r3} - \gamma \qquad\qquad \text{(A.6a)}$$
$$= 0 \qquad\qquad \text{(A.6b)}$$

$$FF = (t_c - x_3 + x_4) \qquad\qquad \text{(A.7)}$$

By solving the equations for the coordinates, one finally find the values for the front focus. Depending on the incoming beam height, the front focus is still a bit different, although the value converges to a certain value. A value of 150.49 mm was found for the front focus of the AC-508-150B lens. For the AC254-200B the front focus was 175.78 mm.

B

Aligning setup

For the final setup to work as proper as possible, different setups and procedures were used.
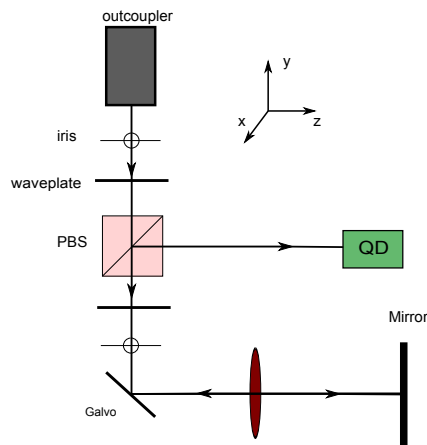

Figure B.1: Setup aligning the first lens in 3 directions: in x and y-direction and such that galvo is at focus of the lens.

Install and align first lens:

- check by eye if the beam hits approximately the center of the lens,

- keep height in mind and remove the lens again

- put the QD such that the beam hits the center

- put the lens in between, adjust y and x direction till signal on QD is same as before

Put the lens such that its focus hits the center of the galvo

- Put a mirror after lens such that it reflection goes back through both irises see figure B.1b).

- Put the QD after cube and center it without oscillating the galvo

- Oscillate the Galve and adjust the position of the lens until oscillation is minimal

In this case we used the following distances:

- Cube and galvo; 21.2 cm

- Cube and QD; 42.2cm

- Lens and mirror; 14.5cm

There should be kept in mind that the cube makes the light beam less stable, because of the polarization change that is produced by the cube.

C

Thick lens

The method of finding the front focus of appendix A is equivalent to how the path was calculated with three lenses. The values of the setup are given in table C.1.

Table C.1: The values of the properties of the achromats.

first achromats	[mm]	third achromat	[mm]
R1	112.21	R1b	106.4
R2	95.94	R2b	96.6
R3	325.1	R3b	2000
tc1	8.2	tc2b	4
tc2	5	tcb	8
BF	145.148	BF2	194.8
FF	150.49	FF2	175.88
n1	1.78559	n1b	1.71233
n2	1.64325	n2b	1.64325

D

Design PI-controller

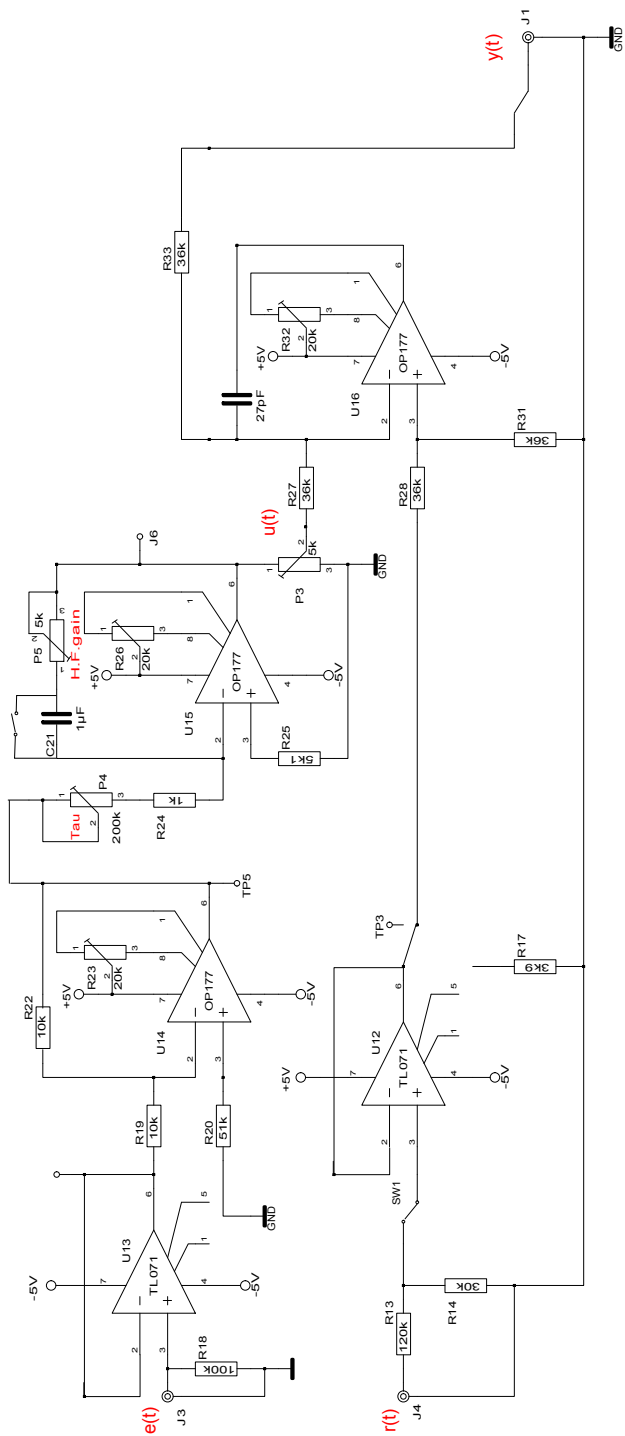The board of the PI-controller, with the used values for the capacitors and resistors.

Figure D.1: Scheme of the PI-controller